A New Model of Moisture Evaporation in Composite Materials in Rapid Temperature Rise Environments

by

David Seechung Tai

B.S., University of California, Berkeley, Berkeley, CA

(1990)

Submitted to the Department of Aeronautics and Astronautics

in partial fulfillment of

the requirements for the degree of

Master of Science

in Aeronautics and Astronautics

at the

Massachusetts Institute of Technology

February 1994

Signature of Author _____

Department of Aeronautics and Astronautics

November 12, 1993

Certified by _____

Professor Hugh L.N. McManus

Thesis Supervisor

Accepted by _____

Professor Harold Y. Wachman

Chairman, Departmental Graduate Committee

A New Model of Moisture Evaporation in Composite Materials in Rapid Temperature Rise Environments

by

David Seechung Tai

Submitted to the Department of Aeronautics and Astronautics on November 12, 1993 in partial fulfillment of the requirements for the Degree of Master of Science in Aeronautics and Astronautics

Abstract

The evaporation of absorbed water has been shown to be a critical factor in the failure of composite material ablators. A new release rate equation to model the phase change of water to steam in composite materials is derived from the theory of molecular diffusion and equilibrium moisture concentration. The new model is dependent on internal pressure, the microstructure of the voids and channels in the composite materials, and the diffusion properties of the matrix material. Hence, it is more fundamental and accurate than the empirical Arrhenius rate equation currently in use. The model and its implementation into the thermostructural analysis code CHAR are described. Parametric studies on variation of several parameters have been done. Comparisons to Arrhenius and straight-line models show that the new model produces physically realistic results under all conditions.

Thesis Supervisor: Professor Hugh L.N. McManus

Title: Assistant Professor of Aeronautics and Astronautics

Acknowledgment

First, I would like to thank Prof. McManus for providing me with the original idea of moisture diffusion to pore channels. Without that idea this work would have gone nowhere. I would also like to thank him for his continuous help, support and encouragement during this work, and assistance and advice on writing this thesis. From him I learned much invaluable knowledge.

This work was partially supported by a grant from NASA Marshall Space flight center, grant # NA68-295.

Finally, I would like to thank my father, mother and aunt for their emotional and financial support.

Table of Contents

List of Figures

List of Tables

Nomenclature

b	constant in equilibrium moisture concentration
c	moisture concentration (kg/m^3)
c_{max}	maximum moisture concentration (kg/m^3)
c_∞	equilibrium moisture concentration (kg/m^3)
d	moisture diffusivity (m^2/s)
d_0	pre-exponential factor of moisture diffusivity (m^2/s)
f	equilibrium degree of conversion
$g()$	a function, Eq. 4-26 (s)
h_x	enthalpy of substance x (J/kg)
h	heating rate (K/s)
mf_g	mass flux of gases (kg/m^2·s)
n	number of pore channels per unit area (1/m^2)
$p()$	a function, Eq. 4-49 (-)
q_{cond}	conduction heat flux (W/m^2)
q_{conv}	convection heat flux due to gases (W/m^2)
r	radial distance (m)
r_a	radius of moisture diffusion control volume (m)
r_p	pore radius (m)
s	sum of moisture concentration per unit length in the control volume (kg/m)
t	time (s)
u, v	auxiliary variables of time (s)
x, y	auxiliary coordinates
x	auxiliary variable
$y_n()$	n^{th} mode shape
z	distance (m)

z_n characteristic value for mode n

A rate constant (1/s)

B, B' some constants

C degree of conversion

C_c degree of conversion of pyrolysis reaction

C_n constant of mode n

Cp_x specific heat of substance x (J/kg·K)

C_u degree of conversion of moisture for $f = 0$ case

C_w degree of conversion of moisture

D_n constant of mode n

E internal energy (W/m^3)

E_a activation energy of Arrhenius rate equation (J/kgmole)

E_{gen} heat generated (W/m^3)

E_n constant of mode n

E_w activation energy for moisture diffusivity (J/kgmole)

G gas generation (kg/m^3·s)

H thickness of insulation (m)

K thermal conductivity (W/m·K)

M molecular weight of gases (J/kgmode)

N number of rate equations used to model the pyrolysis

P pressure (Pa)

P_0 external pressure (Pa)

P_{ave} average pressure (Pa)

P_{max} maximum pressure (Pa)

P_{sat} saturation pressure of water (Pa)

P_v vapor pressure (Pa)

$\hat{Q}$ heat released by reaction (W/m^3)

Q effective heat released by reaction (W/m^3)

R_g universal gas constant (= 8.314 J/kgmole·K)

R_{zz} out-of-plane normal stress ratio (stress/failure stress)

T temperature (K)

T_b beginning temperature of reaction (K)

T_e ending temperature of reaction (K)

V_D Darcy velocity of gases (m^2/s)

α radius ratio

β degree of reaction

β_c degree of char

β_w degree of dry-out

ϕ porosity

γ diffusivity (m^2)

λ_n spatial frequency for mode n (1/m)

μ viscosity (Pa·s)

ρ_x density of substance x (kg/m^3)

τ mechanical stresses (Pa)

τ^e effective stresses (Pa)

ω_{ij} pressure stress coupling factor

Φ ply angle

Θ fiber angle

Subscripts

0 initial variable

c char

g all gases (pyrolysis gases and steam)

p pyrolysis gases

s undegraded solid

v	steam
w	water or moisture
n	n^{th} mode
$,i$	time step i
$,j$	time step j

1 Introduction

1.1 Ablative liner materials

Unlike liquid propellant rockets, where regenerative cooling is available, solid propellant rockets like those used in the Space Shuttle require ablative liner materials for thermal protection. These liners protect the structural material outside from the high temperature gases inside, while the structural material outside carries all the nozzle's pressure load. They are usually built from carbon-phenolic composite materials, because they are light in weight and low in thermal conductivity. Furthermore, because they are strong, they have good resistance to wear caused by the flowing gas inside the nozzle.

The nozzle insulation has a cone shape, but it is usually modeled as a flat plate because the thickness of the insulation is much smaller than the radius of the nozzle. The basic geometry of a flat plate of insulation with thickness H is shown in Figure 1. The insulation is made up of many plies of fiber cloth, which are at angle Φ to the horizontal (x-y) plane. The warp fibers in the ply are oriented at angle Θ, measured in the plane of the ply, to the x-z plane.

1.2 Reaction zones

When the composite liner materials are exposed to the high temperature environment inside a rocket nozzle, different reaction zones develop as shown in Figure 2. First, the material on the heated side will begin to decompose and form a pyrolysis zone. When the decomposition finishes, it leaves a layer of char behind. As more heat conducts into the material, the pyrolysis zone advances deeper into the virgin material. Ahead of the pyrolysis zone, trapped moisture in the virgin material is released. A moisture evaporation zone will also develop and advance ahead of the pyrolysis zone in lower temperature material. If other absorbed

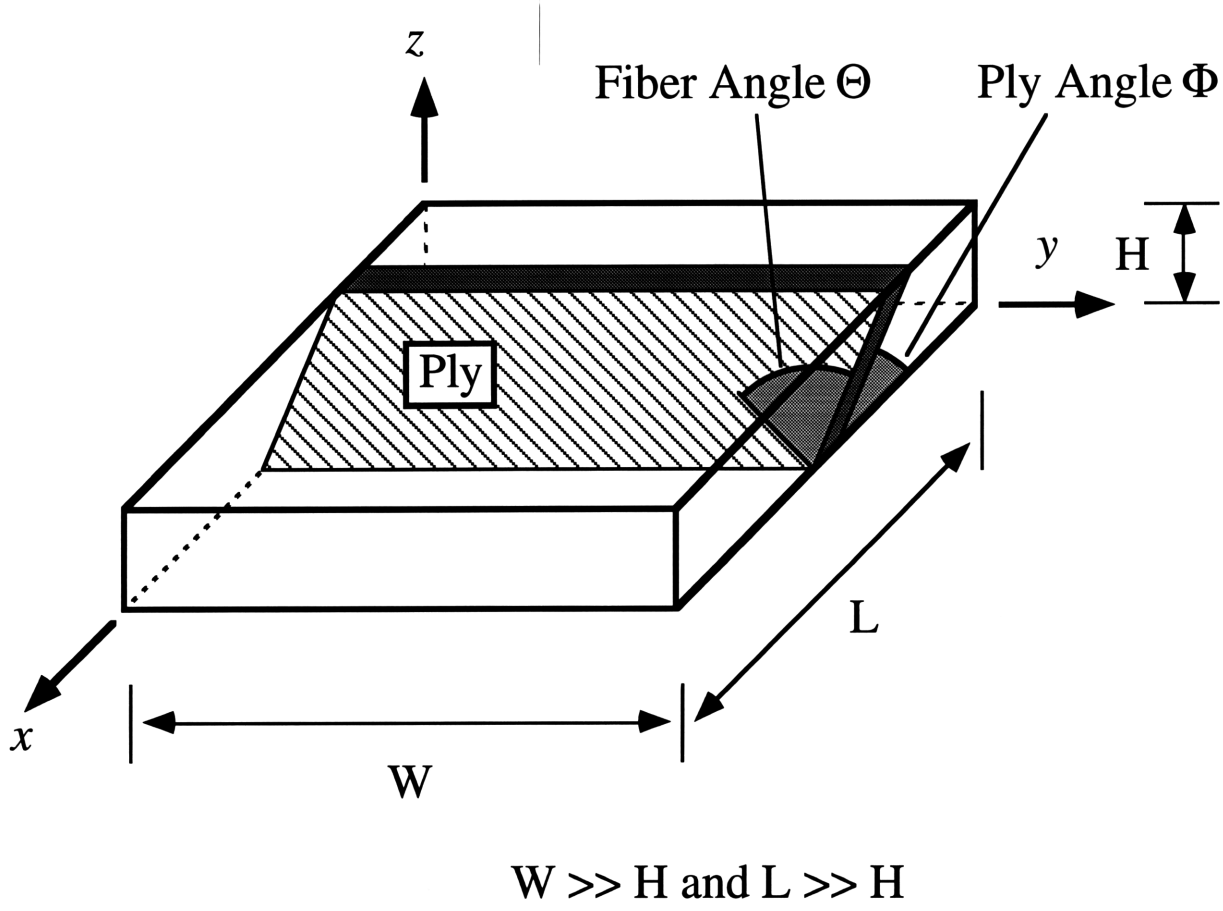

Figure 1. The geometry of ablative insulation.

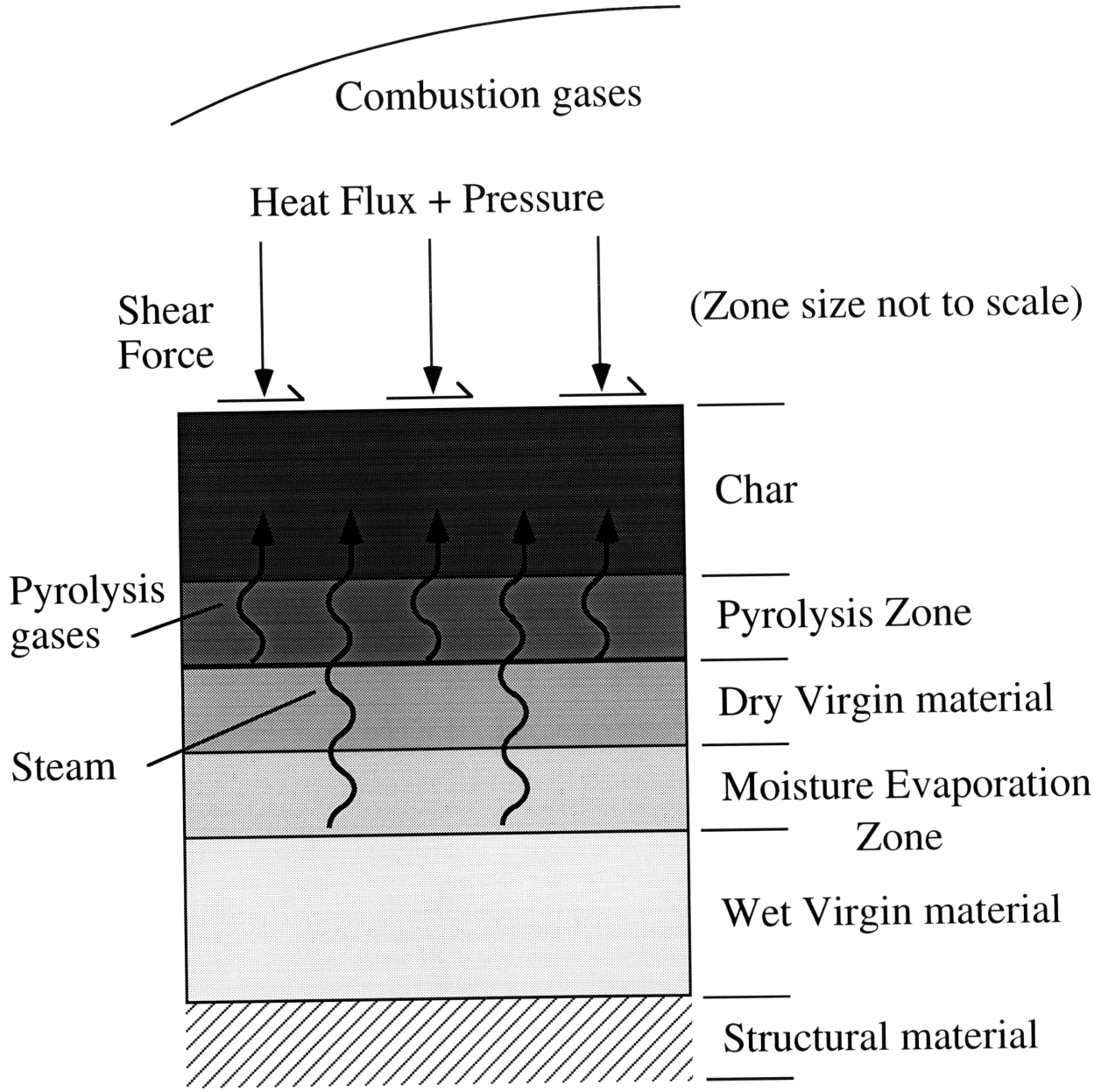

Figure 2. Classification of the reaction zones.

substances such as carbon dioxide are present, they will also form a desorption zone like the moisture evaporation zone. Gases, which are produced by pyrolysis decomposition and moisture evaporation, flow to the surface and provide some cooling, but can cause large internal pressure.

1.3 Ply-lift failure mode

The thickness of the composite insulation is designed so that the char layer will not reach the back side of the material before the rocket engine is shut down. However, several anomalous events can occur during the flight which can cause the insulation to fail prematurely. One of the severe anomalies is known as "ply-lift". Ply-lift refers to the across-ply failure of the matrix material and it has been observed in the exit cone liners of post-fired rocket engines. When it occurs, layers of ply become separated and the plies above the failure region "lift" up as shown in Figure 3. This damages the strength of the composite. Due to the shear force caused by the flowing gas on the surface, the plies above the failure region will eventually tear out. Then, more heat flux is able to pass through the insulation and may damage the structural material. In the worst case, the structural material fails and the whole nozzle may just blow apart. The ply-lift failure usually occurs in the region just underneath the pyrolysis zone, and is more common in composite materials with low angle Φ [1].

1.4 Suggesting mechanisms

The ply-lift failure has been attributed to the following mechanisms. When the material is heated rapidly, gases are generated and trapped. These excess gases cause a large increase in internal pressure which forces the plies apart. Since ply-lift usually occurs in carbon-phenolic composite materials at temperatures below 400 °C and pyrolysis reactions usually do not begin below 400 °C [1], it is suspected that the high internal pressure is mainly caused by steam released by absorbed

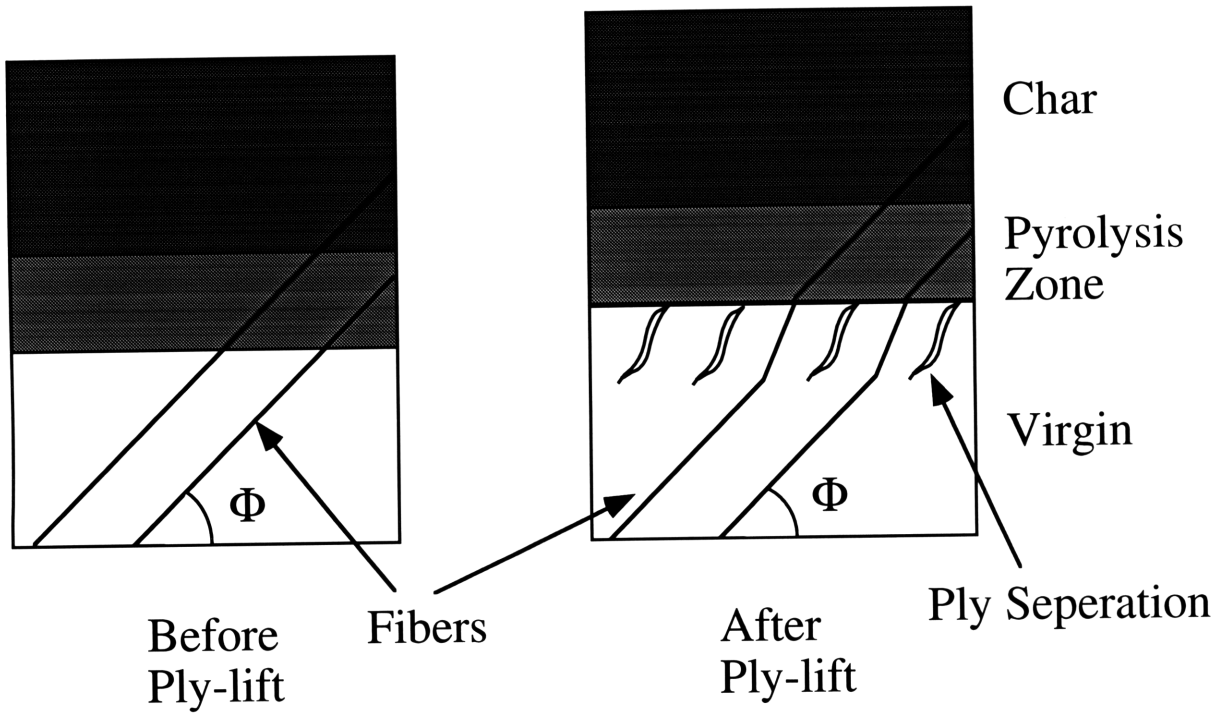

Figure 3. Ply-lift at low angle of Φ.

water. When the matrix material in the composite decomposes to char, the material's permeability can increase by as much as seven orders of magnitude. Thus, the pyrolysis gases inside the pyrolysis zone can escape easily, while steam released in the evaporation zone has more difficulty escaping since it has to pass through the relatively impermeable virgin material between the pyrolysis and moisture evaporation zones. Large internal pressure is built up by gases trapped between these zones, and it is this narrow region where ply-lift failure usually occurs. Since the ply-lift failure is caused by high internal pressure, better modeling of the moisture evaporation process will result in more accurate prediction of the internal pressure and ply-lift failure.

1.5 Gas generation equation

In general, a chemical reaction rate can be modeled by n-th order Arrhenius rate equation.

$$\frac{dC}{dt} = -AC^n exp(\frac{E_a}{R_g T}) \tag{1-1}$$

where C is the degree of conversion, A is the rate constant, n is the order of reaction, E_a is the activation energy, R_g is the universal gas constant, and T is the absolute temperature. $C(0)$ equals 1 and C approaches 0 as time goes to infinity. The degree of reaction is

$$\begin{aligned} \beta &= 1 - C \\ \frac{d\beta}{dt} &= -\frac{dC}{dt} \end{aligned} \tag{1-2}$$

The Arrhenius rate equation is not dependent on pressure, but the boiling point of water is. To model a temperature and pressure dependent moisture evaporation rate equation, McManus [2] proposed a simple straight-line model in which the reaction rate is constant.

$$C_w = \begin{cases} 1 & for\ T < T_b \\ \dfrac{(T_e - T)}{(T_e - T_b)} & for\ T_b < T < T_e \\ 0 & for\ T_e < T \end{cases} \tag{1-3}$$

$$\frac{dC_w}{dt} = \begin{cases} -\dfrac{1}{(T_e - T_b)}\dfrac{dT}{dt} = -\dfrac{1}{\Delta T}\dfrac{dT}{dt} & for \quad T_b < T < T_e \\ 0 & for\ T < T_b\ or\ T_e < T \end{cases} \tag{1-4}$$

where T_b is the boiling point of water and T_e equals T_b plus an empirical constant ΔT. Another method he proposed is an Arrhenius equation with E_a as a function of pressure [3]. However, both methods are empirical. There is no guarantee that they predict an accurate moisture evaporation rate and they provide no insight into rate determining mechanisms. So in this study, a new moisture evaporation model based on a more fundamental and physical modeling of moisture diffusion and equilibrium moisture concentration is derived to improve the accuracy of predicting the moisture evaporation rate. This model will be coupled into an existing thermo-chemical-structural analysis program to provide a new and more accurate tool for predicting the behavior of ablative composite materials.

1.6 Thesis outline

In the following Chapter 2, previous work on this problem will be reviewed and current analytical modeling techniques will be presented. Chapter 3 will give a precise problem statement. Chapter 4 will describe the derivation of the new rate equation. Chapter 5 will present the results of parametric studies, and discuss the importance of the new rate equation. Chapters 6 and 7 will present conclusions and recommendations.

2 Background

2.1 History

The earliest work on the pyrolysis of composite materials were done on wood for fire-retarding purposes (see [4] for more early history). In 1968, Moyer and Rindal [5] investigated the thermal response of man-made composite materials, which were used as charring ablator heat shields on re-entry vehicles.

In the early 80's, Henderson and colleagues did many experiments to determine the properties of glass-phenolic composite materials. In 1985, Henderson et al. [6] gave a crude model of pyrolysis in composite materials. The model included an Arrhenius reaction model, an energy equation and a steady-state mass flow equation. Then in 1987, the model was refined to include a mass flow equation based on Darcy's law, and the thermal expansion of the solid material [7]. In 1991, Florio and Henderson [8] proposed to use two energy equations, with one temperature for solid material and another temperature for gas, to account for the local heat transfer between the solid material and the gas.

However, Henderson's model dealt with thermal and internal pressure responses only and did not calculate the stress inside the material. Recently, three Ph.D. theses (Kuhlmann [9] in 1991, and McManus [2] and Sullivan [10] in 1990) were written to couple Biot's effective stress theory to the existing thermal, chemical, and gas flow theory so as to predict the material temperature, pressure and stress at the same time. A more unified thermo-poro-elastic theory was purposed by Weiler [11] in 1991. Although each of the authors used different approach to derive the coupled thermo-poro-elastic theory, the McManus model will be used in this study.

In recent years, Stokes and his colleagues have performed many experiments related to the pyrolysis of carbon-phenolic composite materials. They have

performed restrained thermal growth (RTG) and coefficient of thermal expansion (CTE) tests, whose results were used to correlate the numerical results in both Sullivan's and Kuhlmann's papers. They also measured the permeability and moisture diffusion of carbon-phenolic composite materials, and investigated the ply-lift failure, the microscopic structure related to permeability, and the effect of moisture on the composite's strength. In Stokes' 1991 summary report [1], he pointed out the close relationship of closed crenulation channels to permeability. These channels are the basic geometry upon which the new reaction rate equation is based.

2.2 Analytical framework

In most cases, the problem of pyrolysis in composite materials is simplified to one dimension, either z in cartesian or r in cylindrical coordinates, because of complexity of the coupling between thermal, pressure and stress equations. If the external pressure and forces on the surface are uniform in Figure 1, then all variables vary only in the z-direction. Therefore, the following thermal and pressure equations will be given in one dimension (z) only. This simplification is valid for the case of thin plate-like structures.

2.2.1 Thermal equation

The thermal equation is

$$\frac{dE}{dt}+\frac{d}{dz}(q_{cond})+\frac{d}{dz}(q_{conv})=E_{gen} \tag{2-1}$$

where E is internal energy, q_{cond} is heat flux due to conduction, q_{conv} is heat flux due to convection of gases, and E_{gen} is the energy generated by pyrolysis reaction and moisture evaporation. Specifically, the terms are

$$\begin{aligned} \frac{dE}{dt} &= \frac{d}{dt}(\rho_s h_s + \rho_c h_c + \rho_w h_w + \rho_p h_p + \rho_v h_v) \\ q_{cond} &= -K_z \frac{dT}{dz} \\ q_{conv} &= h_g m f_g \\ E_{gen} &= \rho_s \hat{Q}_c \frac{d\beta_c}{dt} + \rho_w \hat{Q}_w \frac{d\beta_w}{dt} \end{aligned} \tag{2-2}$$

where $\rho_{s,c,w,p,v}$ is the density of solid, char, water, pyrolysis gases and steam respectively, $h_{s,c,w,p,v}$ is the enthalpy of solid, char, water, pyrolysis gases and steam respectively, K_z is the thermal conductivity of solid in the z direction, T is the temperature of solid and gases, h_g is enthalpy of gases, mf_g is the mass flow of gases, $\hat{Q}_c$ is the heat generated by pyrolysis reaction, and $\hat{Q}_w$ is the heat generated by moisture evaporation. Also β_c is degree of char (DOC), which varies from 0 (virgin) to 1 (char), β_w is degree of dry-out (DOD), which varies from 0 (wet) to 1 (dry), $\frac{d\beta_c}{dt}$ is the reaction rate of the pyrolysis reaction, and $\frac{d\beta_w}{dt}$ is the release rate of the moisture evaporation. For an exothermic reaction, $\hat{Q}$ is positive.

Assuming ideal gas

$$dh_{p,v} = Cp_{p,v} dt \tag{2-3}$$

Equation 2-1 is simplified to

$$\begin{aligned} &\left\{(1-\phi)\left[(1-\beta_c)\rho_s Cp_s + \beta_c \rho_c Cp_c\right] + \phi \rho_g Cp_g\right\}\frac{dT}{dt} = \\ &\frac{d}{dz}(K_z \frac{dT}{dz}) - Cp_g m f_g \frac{dT}{dz} + \rho_s Q_c \frac{d\beta_c}{dt} + \rho_w Q_w \frac{d\beta_w}{dt} \end{aligned} \tag{2-4}$$

where ϕ is the porosity, ρ_s is the density of solid, ρ_g is the density of gases, Cp_s is the specific heat of solid, Cp_c is the specific heat of char, Cp_g is the specific heat of gases, and Q_c and Q_w are effective heat of pyrolysis and moisture evaporation, which are

$$\begin{aligned} Q_c &= \hat{Q}_c + h_s - \frac{\rho_c}{\rho_s} h_c - (1 - \frac{\rho_c}{\rho_s}) h_p \\ Q_w &= \hat{Q}_w + h_w - h_v \end{aligned} \tag{2-5}$$

2.2.2 Mass flow equation

Gas is assumed to flow according to Darcy's equation [12], in which the velocity of gas (or fluid) V_D is determined by the permeability constant γ, viscosity μ and pressure gradient dP/dz

$$V_D = -\frac{\gamma}{\mu}\frac{dP}{dz} \tag{2-6}$$

Then the mass flux of gases is

$$mf_g = \rho_g V_D \tag{2-7}$$

The mass continuity equation is

$$\frac{d(\phi\rho_g)}{dt} + \frac{d}{dz}(mf_g) = G_g = G_p + G_v \tag{2-8}$$

where G_g is the total gas mass generated per unit volume and time, and is given by the sum of the gas mass generated by pyrolysis and the mass of the steam generated by moisture evaporation. The first term of Eq. 2-8 represents the mass storage term, the second represents the change of mass flow, and the last term represents the gas generation. Other authors [9-11] include porosity ϕ dependence on the material strain, causing coupling between the mass flow equation and stress equation. However, Sullivan [13] compared two cases with and without the porosity dependence on the material strain. He found out that the difference is very small, so we neglect the porosity dependence on the material strain here.

In steady state, Eq. 2-8 can be simplified to

$$\frac{d}{dz}(mf_g) = G_g \tag{2-9}$$

Given that $mf(0)$=0

$$mf_g(z) = \int_0^z G_g(s)ds \tag{2-10}$$

Combining Eq. 2-10, Eq. 2-7 and Eq. 2-6 yields

$$\frac{dP}{dz} = -\frac{\mu}{\gamma}\left(\frac{1}{\rho_g}\right) m f_g(z) \tag{2-11}$$

The density of gases is determined by ideal gas law

$$\rho_g = \frac{M}{R_g T} P \tag{2-12}$$

where M is the mean molecular weight of gases and R_g is the universal gas constant. Equations 2-10 and 2-11 can be solved to find the internal pressure if the gas generation rate is known. However, the gas generation rate is dependent on temperature and possibly internal pressure. This causes coupling between the thermal and mass flow equations. Hence both temperature and internal pressure have to be solved for simultaneously.

For the pyrolysis reaction, the reaction rate can be accurately modeled by one or more Arrhenius rate equations (Eq. 1-1). Then the pyrolysis gas masses generated are

$$G_p = \sum_{i=1}^{N} \Delta m_i \frac{d\beta_i}{dt} = -\sum_{i=1}^{N} \Delta m_i \frac{dC_i}{dt} \tag{2-13}$$

where Δm_i is the total amount of gas released in each reaction i and N is the number of rate equations used to model the pyrolysis. However, moisture evaporation is dependent on pressure. Two methods to model this dependence have already been described in Section 1.5. Both McManus [3] and Kuhlmann [9] have stressed two critical factors in modeling of this problem:

1) the rate of moisture evaporation

2) the permeability of the composite materials

Accurate gas mass generation models as well as an accurate permeability opening model are needed to accurately predict internal pressure. The modeling of moisture evaporation is the primary focus of this work.

2.2.3 Stress equation

McManus [2] used Biot's effective stress theory [14] to predict the stress caused by internal pressure. Biot's theory defines an effective stress as

$$\tau_{ij}^{e} = \tau_{ij} - \omega_{ij} P \tag{2-14}$$

where τ_{ij}^{e} is the effective stress, τ_{ij} is mechanical applied stress, ω_{ij} is the coupling factor, and P is the pressure. This effective stress can in turn be used to predict the direction of material failure by a maximum stress failure criteria. If across-ply tensile stresses exceed the material strength, the matrix fails and ply-lift will occur. If with-ply normal stresses exceed the material strength, the fiber fails and the whole chunk of plies above the failure will become separated at once. The coupling factor ω_{ij} is depended only on the microstructure of voids in the materials.

2.3 CHAR computer code

These equations were incorporated into McManus's CHAR computer code [2]. Complete descriptions of the CHAR code can be found in his paper. He studied the FM5055 carbon-phenolic composite material, measured its permeability as a function of degree of char from experiments, and used its properties as an input to the CHAR code.

A typical case study uses a plate with 3 cm height, 45 degree Θ, 15 degree Φ, and initial moisture content 3.5% as an input to CHAR. The straight-line model is used for both pyrolysis and moisture evaporation. The boundary conditions use a simplified rocket nozzle service environment, which is shown in Figure 4. The external temperature and pressure will rise to 3000 K and 10 MPa respectively after the rocket ignites. At 100 sec, the rocket motor is shut off and the external temperature and pressure are assumed to ramp down in 5 sec to 300 K and 0.1 MPa respectively. CHAR outputs the temperature, internal pressure, mass flow, degree of char, degree of dry-out, and stresses. The temperature history is shown in

Figure 5. The maximum pressure difference (internal pressure minus external pressure) and the stress ratio R_{zz} at the failure location are shown in Figure 6. The failure location is just ahead of the char zone. At shut off, the external pressure drops suddenly, causing an increase in the pressure difference and hence the stress. As indicated by the spike in Figure 6, the stress ratio exceeds one at shut off so the matrix material fails. The results from CHAR numerically replicate a ply-lift failure after motor shut off. However, if the internal pressure rises faster than in this example case, ply-lift failure can occur before shut off, which could cause premature nozzle failure. Increased internal pressure rise can be caused by variation of many parameters: lower permeability, smaller angle Φ, higher initial moisture content (for carbon-phenolic composite material, the maximum moisture content can be as high as 8%), lower external pressure, etc.

Figure 7 shows profile plots of pressure, mass flow of gases, degree of char and degree of dry-out, and indicates the importance of the two critical factors: accurate prediction of moisture release rate and material permeability. Although the amount of steam released is small, it causes about 2.5 MPa of pressure rise as compare to about 2.0 MPa of pressure rise due to pyrolysis gases. The reason is that steam has to escape through the relatively impermeable virgin material. Also, most of the pressure rise due to pyrolysis gases in the pyrolysis zone is near the beginning of pyrolysis, where material permeability is still relatively small. The pyrolysis gases released near the end of pyrolysis cause negligible pressure rise. How the material permeability changes from virgin to char will affect the prediction of pressure rise due to pyrolysis gases and steam. In this work, we will primarily focus on deriving a new model of moisture evaporation to accurately predict the moisture release rate.

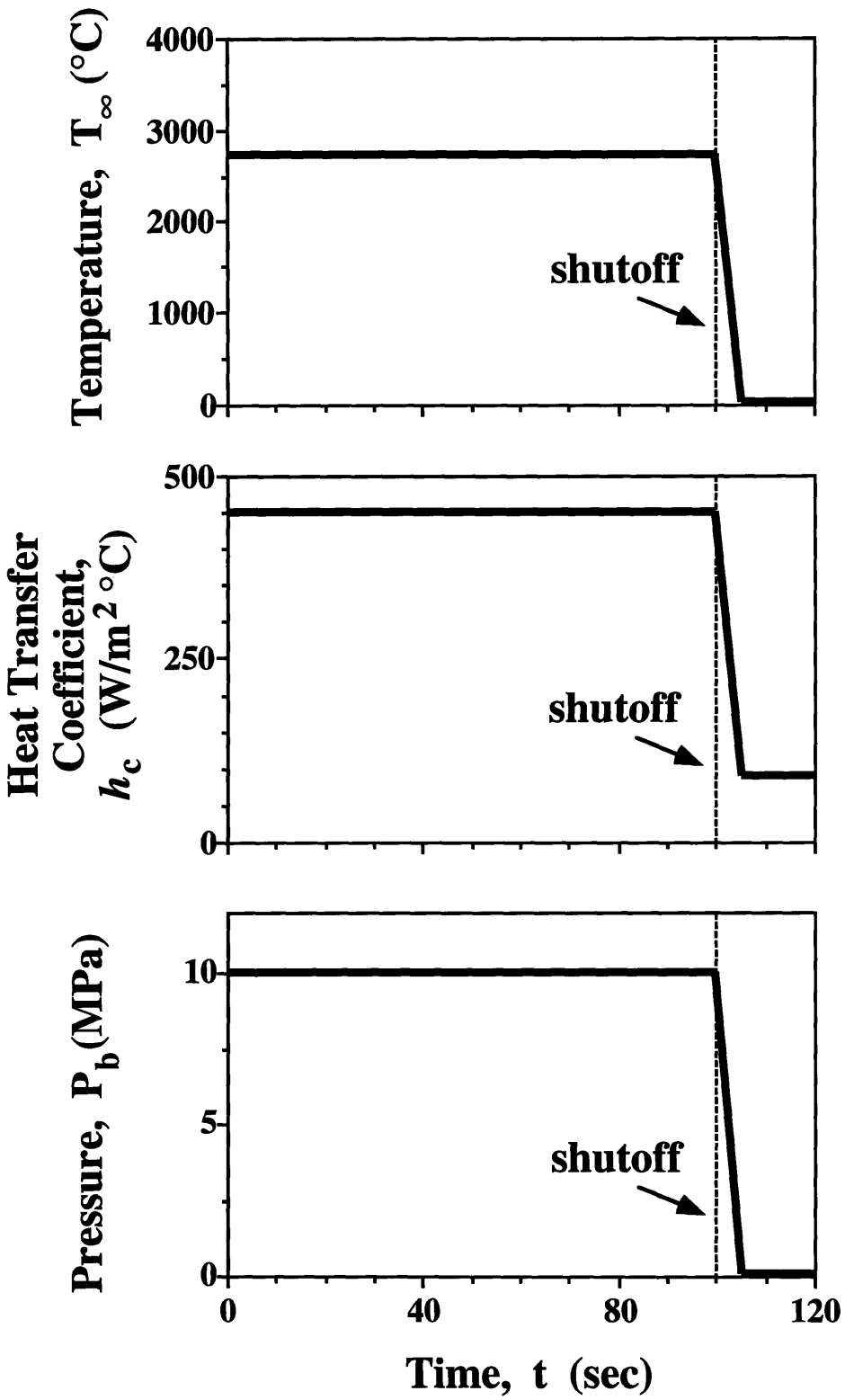

Figure 4. Boundary conditions used in CHAR.

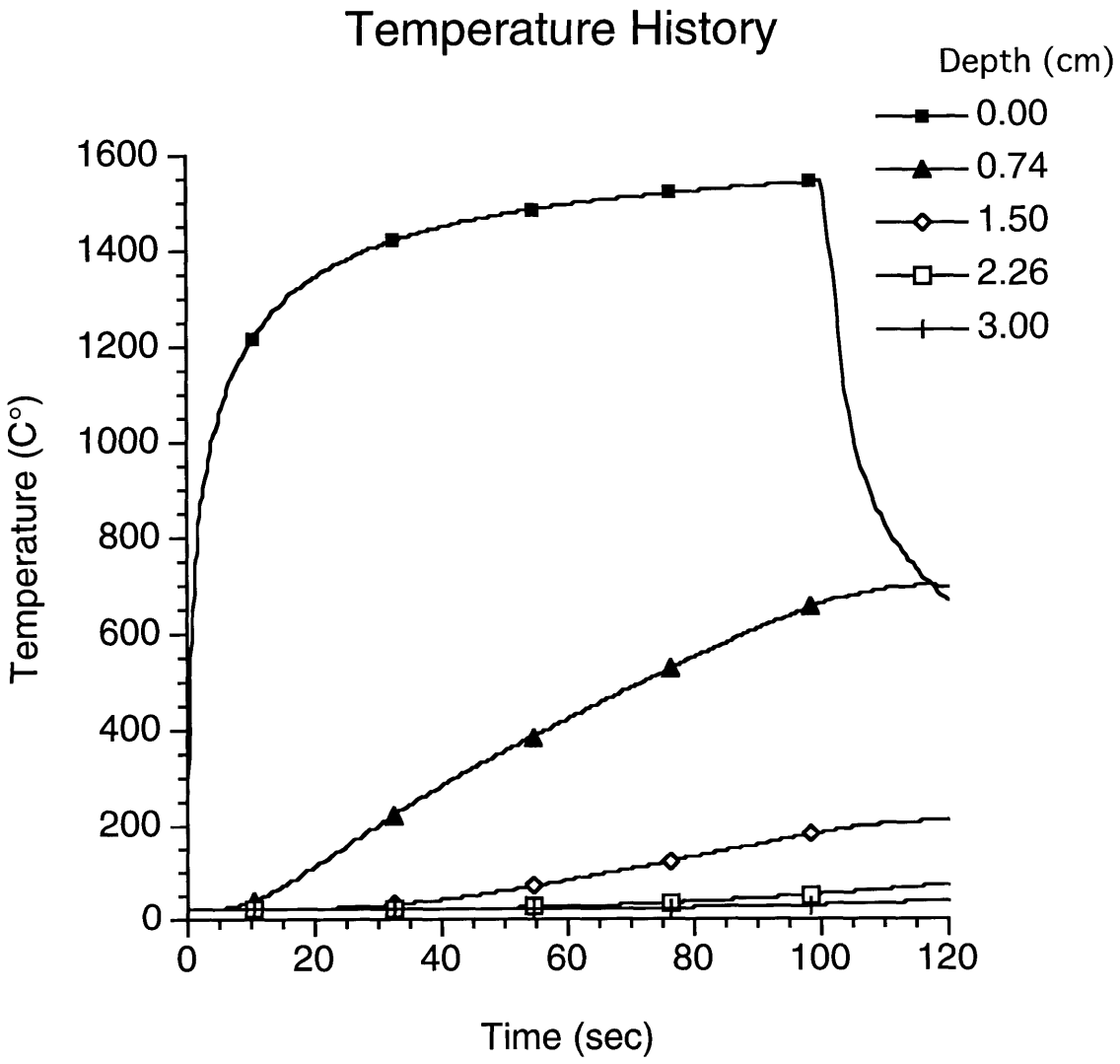

Figure 5. Temperature history plot.

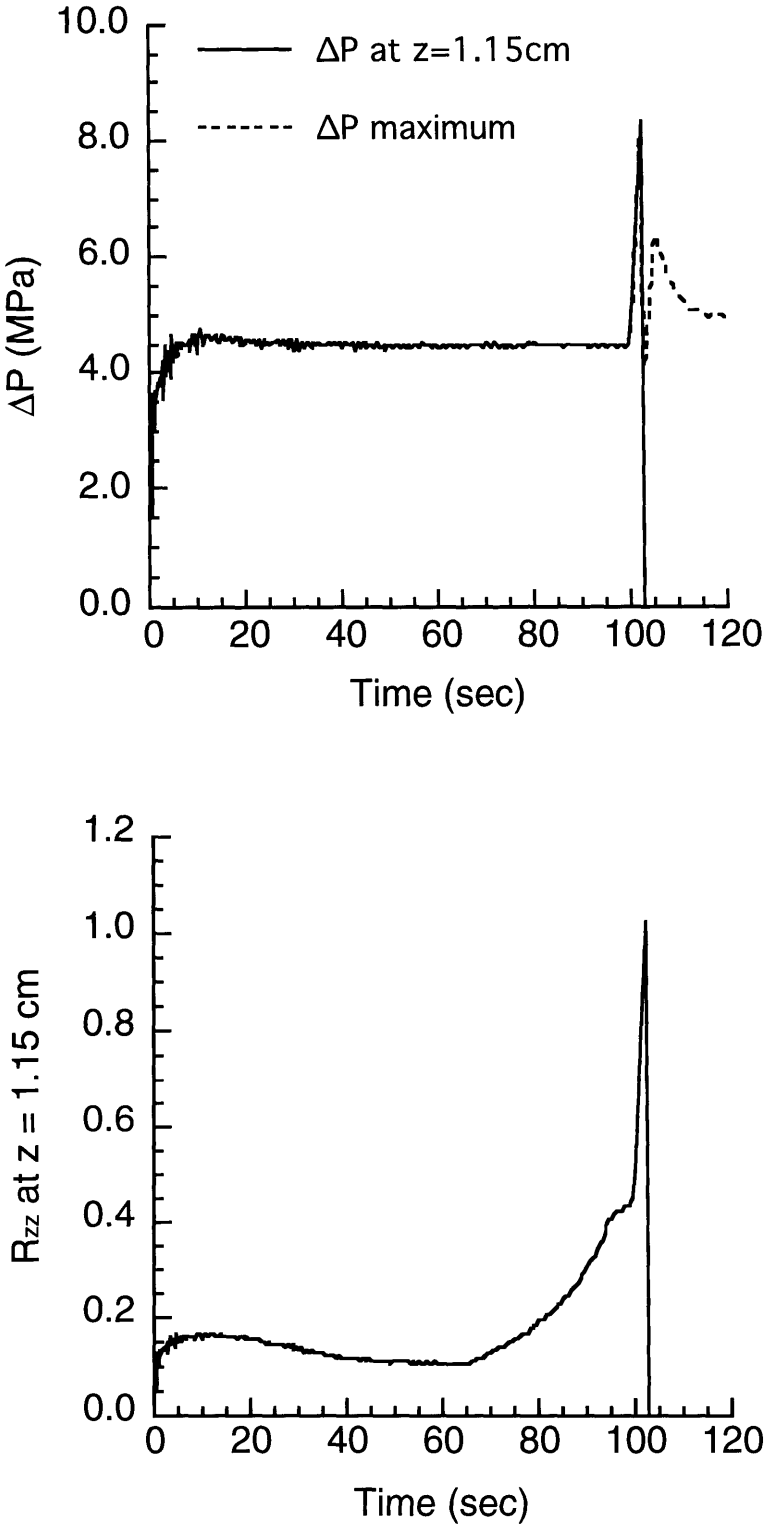

Figure 6. Pressure difference and stress ratio at z = 1.15 cm.

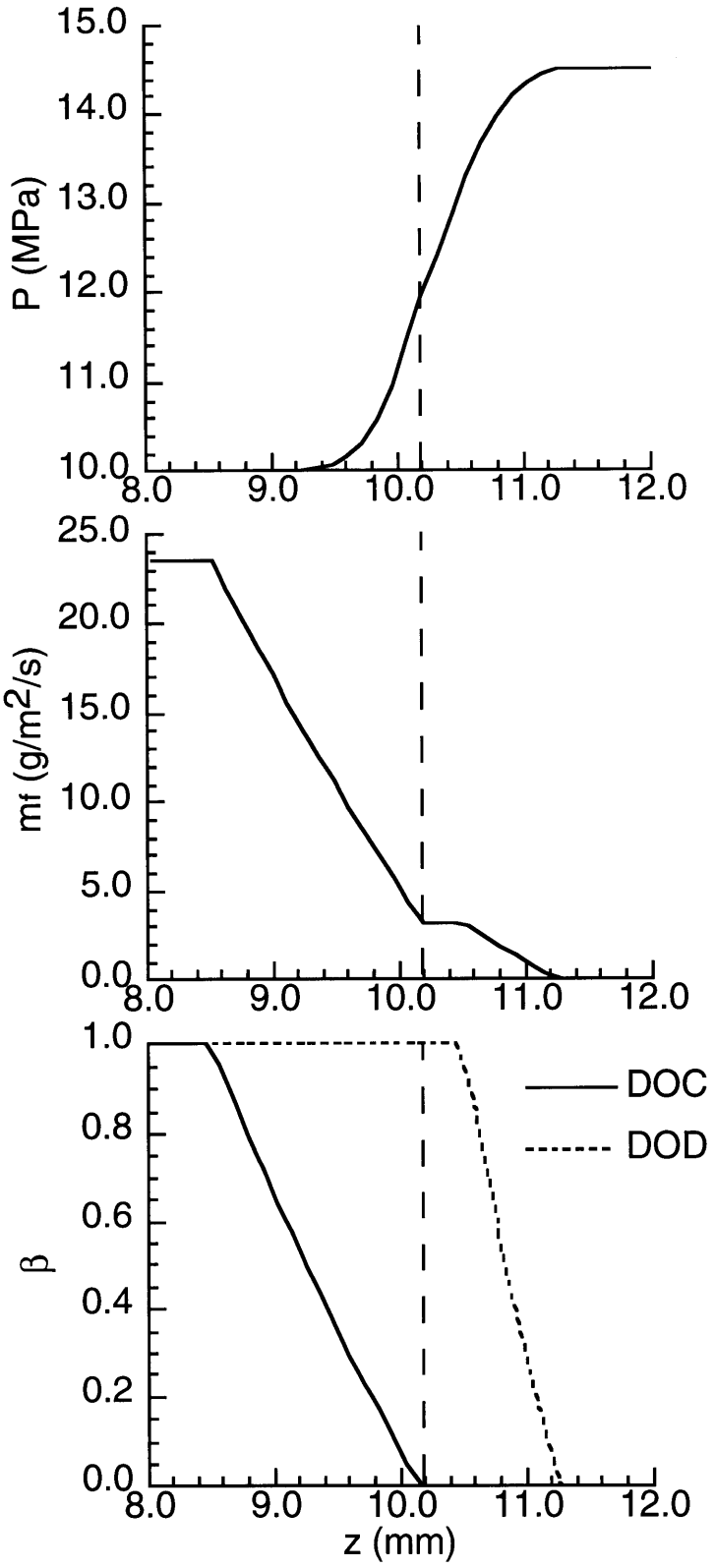

Figure 7. Profile plot of Pressure P, mass flow mf, degree of char (DOC) β_c and degree of dry-out (DOD) β_w.

3 Problem statement

Although the service life of composite materials used as ablative heat shields can be determined experimentally, such experiments must be done on a large scale to give accurate results. Since many composite materials are under development to be used as insulating materials, full scale experiments on even samples of them will be prohibitively costly. Moreover, experiments do not always reveal the details of underlying physical processes. Therefore, accurate equations to model the actual physical processes inside composite materials should be sought so that the design and evaluation of the materials can be aided and directed confidently by numerical codes.

The design of thermal protection structure requires accurate prediction of failure modes such as ply-lift failure. It has been shown that this prediction depends on an accurate release rate equation for moisture evaporation. A new moisture release rate equation will be developed which models the physical processes of molecular diffusion of moisture to the surface of a nearby pore channel, and the release of moisture (stream) into the channel.

For a given initial moisture content, diffusivity constants, and pore channel geometry, we will predict the release rate of moisture to steam as a function of temperature and time. The new rate equation will be incorporated into the existing CHAR code. Coupling the new rate equation to the thermal, mass continuity and stress equations in CHAR, we will determine pressure, stress and failure, if any.

4 Theory

4.1 Overview

The new reaction rate equation for moisture evaporation will be derived from a microscopic point of view. First, we assume moisture is uniformly distributed within the material. Then the moisture must diffuse to a nearby pore channel, driven by the difference in concentration, as shown in Figure 8. The pore channel is either a long crack along the fiber-matrix interface or a closed crenulation channel inside a fiber [1]. More specifically, the moisture will evaporate at the pore channel's surface and become steam. How much moisture evaporates at the surface is determined by the equilibrium moisture concentration, which depends on the temperature and vapor pressure inside the pore channel. Since moisture evaporation on the surface at high temperature is very fast, we assume the surface will achieve equilibrium instantly. Then steam will escape by flowing through the pore channel, driven by pressure difference. A schematic of the moisture release process is shown in Figure 9.

4.2 Moisture diffusion

The moisture diffusion is governed by Fick's diffusion law [15].

$$\nabla \cdot (d \nabla c) = \frac{dc}{dt} \tag{4-1}$$

where d is the moisture diffusivity, c is the moisture concentration (the mass of moisture inside the materials divided by the mass of dry materials), and ∇ is the del operator. The diffusivity d is given by

$$d = d_0 \exp(-\frac{E_w}{R_g T}) \tag{4-2}$$

where d_0 is a pre-exponential factor and E_w is the activation energy. Fick's diffusion

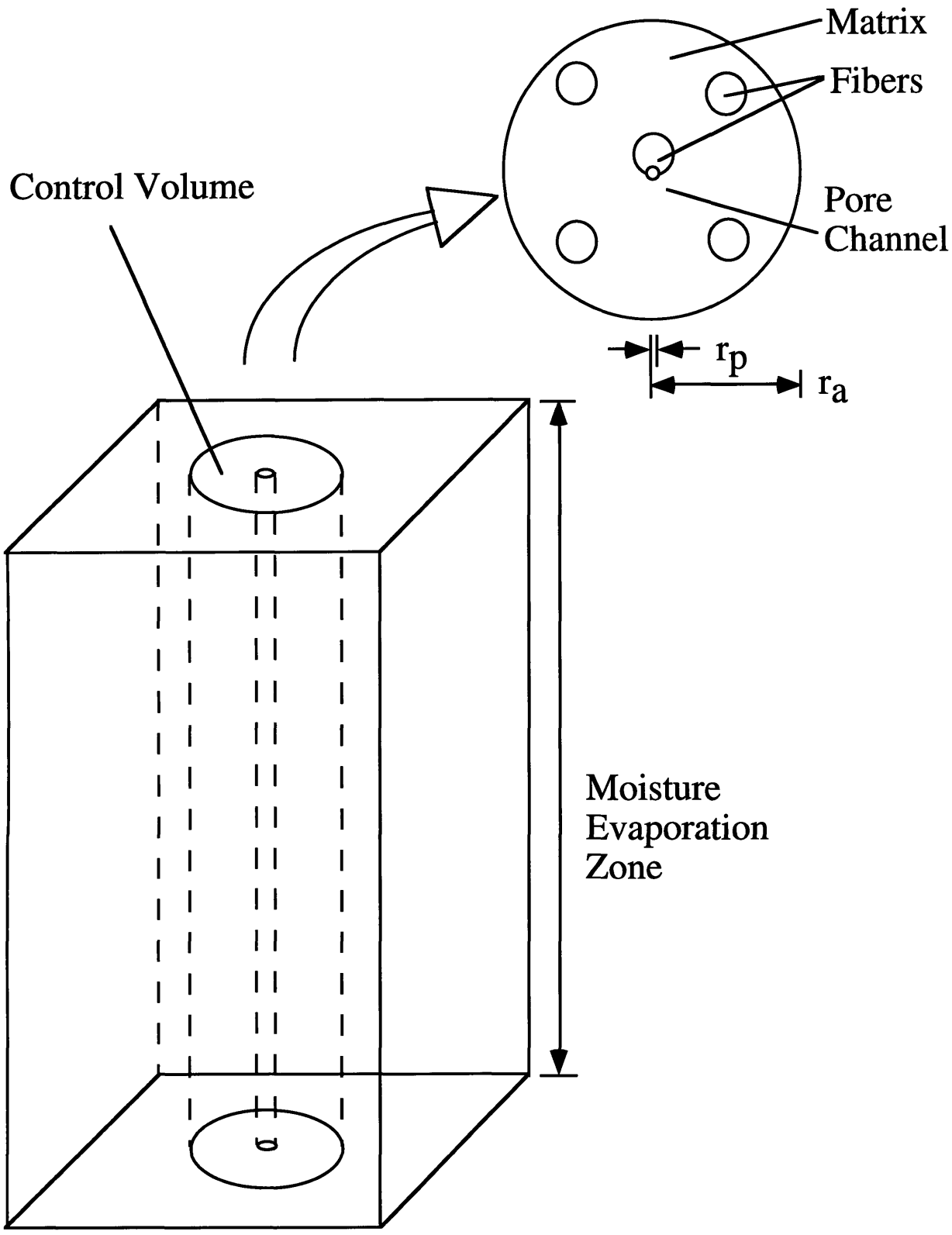

Figure 8. The geometry of the diffusion area of one pore channel.

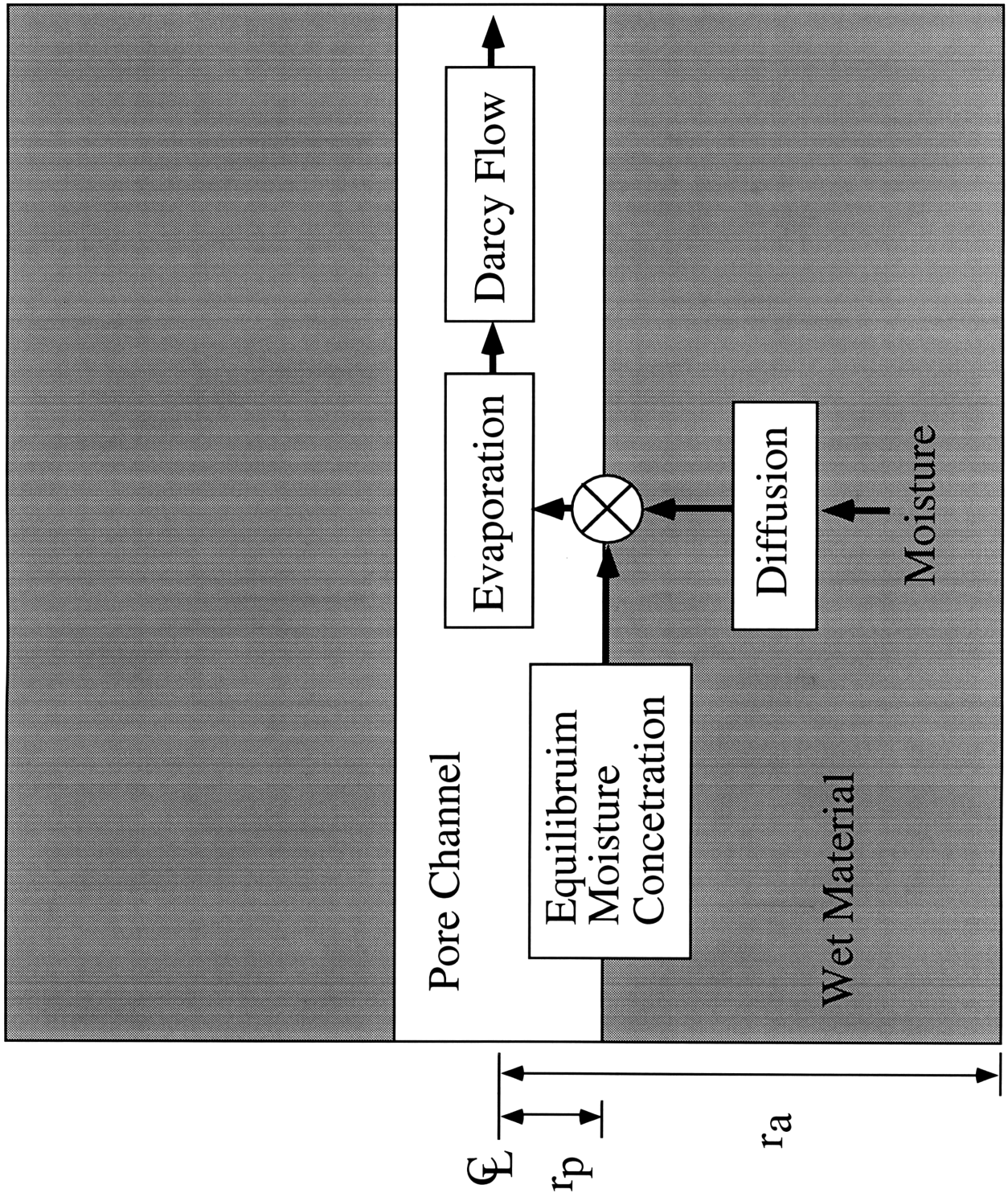

Figure 9. Schematic of reaction rate.

law is very similar to Fourier's heat conduction equation. Both are second order partial differential equations in space and first order differential equations in time.

The moisture control volume as shown in Figure 8 is defined such that all moisture inside the control volume will go to one pore channel. In general, the boundary of the moisture control volume is an irregular polygon. We can approximate this shape by a circle with radius r_a, which is approximately equal to half of the average distance between two pore channels. Although cross sections of pore channels usually have different sizes and irregular shapes, a circle with average radius r_p is also assumed here for easier calculation. We assume that the initial moisture content is uniform inside the materials to smear out the difference of moisture absorption between the fiber and the matrix. Similarly, the fiber and matrix materials around the pore channel are assumed to have a homogeneous effective diffusivity constant. If we assume r_a is less than Δz, where Δz is the node spacing of the numerical calculations, then we can assume the temperature inside any one control volume is constant so that moisture diffusivity is constant everywhere in the control volume. With the same assumption, we can neglect the derivative of c in the z-direction and derive the moisture release rate independent of Φ. These assumptions reduce the problem from three dimensions to one.

The assumptions made so far are:

1) The boundary of control volume is circular with radius r_a.
2) All pore channels are circle of radius r_p.
3) Initial moisture content is uniform within the materials.
4) The materials are effectively homogenous with one diffusivity constant.
5) The temperature inside a control node is constant.
6) The derivative of c in the z direction is zero.

With the above assumptions, Eq. 4-1 is reduced to

$$\frac{1}{r}\frac{\partial}{\partial r}(r\frac{\partial c}{\partial r}) = \frac{\partial^2 c}{\partial r^2} + \frac{1}{r}\frac{\partial c}{\partial r} = \frac{1}{d}\frac{\partial c}{\partial t} \tag{4-3}$$

We assume an initial condition $c = c_0$ and boundary conditions

$$c = 0 \qquad \text{at } r = r_p$$
$$\frac{dc}{dr} = 0 \qquad \text{at } r = r_a$$

such that moisture is zero (equilibrium at vacuum) at the surface of the central pore channel and moisture cannot cross the boundary to other control volumes.

Using separation of variables, let

$$\frac{c(r,t)}{c_0} = R(r)\theta(T) \tag{4-4}$$

Then

$$\frac{R''}{R} + \frac{1}{r}\frac{R'}{R} = \frac{1}{d}\frac{\dot{\theta}}{\theta} = -\lambda^2, \quad \lambda \geq 0 \tag{4-5}$$

where R' indicates the derivative of R with respect to r and $\dot{\theta}$ indicates the time derivative of θ.

For the $R(r)$ part,

$$R'' + \frac{1}{r}R' = -\lambda^2 R \tag{4-6}$$

$$r^2 R'' + rR' + \lambda^2 r^2 R = 0 \tag{4-7}$$

This ordinary differential equation (ODE) is the Bessel differential function of order 0 [16], and the general solution is

$$R(r) = BJ_0(\lambda r) + B'Y_0(\lambda r) \tag{4-8}$$

where B and B' are constants, J_0 is Bessel function of order 0 of the first kind, and Y_0 is Bessel function of order 0 of the second kind. Applying the boundary condition at $r = r_p$, $c(r_p, t) = 0$ so $R(r_p) = 0$. Then Eq. 4-8 becomes

$$BJ_0(\lambda r_p) + B'Y_0(\lambda r_p) = 0 \tag{4-9}$$

The other boundary condition at $r = r_a$ yields $\left.\frac{\partial c}{\partial r}\right|_{r=r_a} = 0$, so $R'(r_a) = 0$. Then Eq. 4-8 becomes

$$-BJ_1(r_a) - B'Y_1(r_a) = 0 \tag{4-10}$$

Solving for B from Eq. 4-9

$$B = -B'\frac{Y_0(\lambda r_p)}{J_0(\lambda r_p)} \tag{4-11}$$

Substituting B into Eq 4-8

$$R(r) = B'\left(-\frac{Y_0(\lambda r_p)}{J_0(\lambda r_p)}J_0(\lambda r) + Y_0(\lambda r)\right) \tag{4-12}$$

Multiplying by $-J_0(\lambda r_p)$, we get

$$R(r) = Cy(r) \tag{4-13}$$

where

$$y(r) = Y_0(\lambda r_p)J_0(\lambda r) - J_0(\lambda r_p)Y_0(\lambda r) \tag{4-14}$$

Substituting B from Eq. 4-11 into Eq. 4-10

$$B'\left(\frac{Y_0(\lambda r_p)}{J_0(\lambda r_p)}J_1(\lambda r_a) - Y_1(\lambda r_a)\right) = 0 \tag{4-15}$$

The constant B' cannot be zero, so we have the characteristic equation

$$J_0(\lambda_n r_p)Y_1(\lambda_n r_a) - Y_0(\lambda_n r_p)J_1(\lambda_n r_a) = 0 \tag{4-16}$$

To simplify this characteristic equation, let

$$\lambda_n r_p = z_n \quad and \quad \lambda_n r_a = \alpha z_n \tag{4-17}$$

where the radius ratio α is

$$\alpha = \frac{r_a}{r_p} \tag{4-18}$$

Then

$$J_0(z_n)Y_1(\alpha z_n) - Y_0(z_n)J_1(\alpha z_n) = 0 \tag{4-19}$$

z_n is solved from Eq. 4-19 numerically for any given α, and λ_n is calculated by Eq. 4-17. Then Eq. 4-13 becomes

$$R(r) = \sum_{n=1}^{\infty} C_n y_n(r) \tag{4-20}$$

where $$y_n(r) = Y_0(\lambda_n r_p)J_0(\lambda_n r) - J_0(\lambda_n r_p)Y_0(\lambda_n r) \tag{4-21}$$

$R(r)$ is represented by the sum of the magnitude C_n times the mode shapes $y_n(r)$. The first five mode shapes of $y_n(r)$ are plotted in Figure 10 for α = 20. The first mode shape is similar to a quarter period of a sine function. The second mode shape is similar to three quarters of a period of a sine function. The third, forth, fifth mode shapes are similar to sine functions with periods 5/4, 7/4 and 9/4, respectively. For the $\theta(t)$ part,

$$\dot{\theta} = -\lambda_n^2 d\theta \tag{4-22}$$

Substituting Eq. 4-2 into Eq. 4-22

$$\dot{\theta} = -\lambda_n^2 d_0 \, exp(-\frac{E_w}{R_g T})\theta \tag{4-23}$$

Integrating both sides from 0 to t

$$\int_{\theta(0)}^{\theta(t)} \frac{1}{\theta} d\theta = -d_0 \lambda_n^2 \int_0^t exp(-\frac{E_w}{R_g T(s)})ds \tag{4-24}$$

$$\theta(t) = \theta(0)exp(-d_0 \lambda_n^2 g(t)) \tag{4-25}$$

where $$g(t) = \int_0^t exp(-\frac{E_w}{R_g T(s)})ds \tag{4-26}$$

Since the initial condition $c(0) = c_0$ and $R(r)$ is assumed to be 1 for $r_p \le r \le r_a$ at t = 0, $\theta(0)$ = 1 and

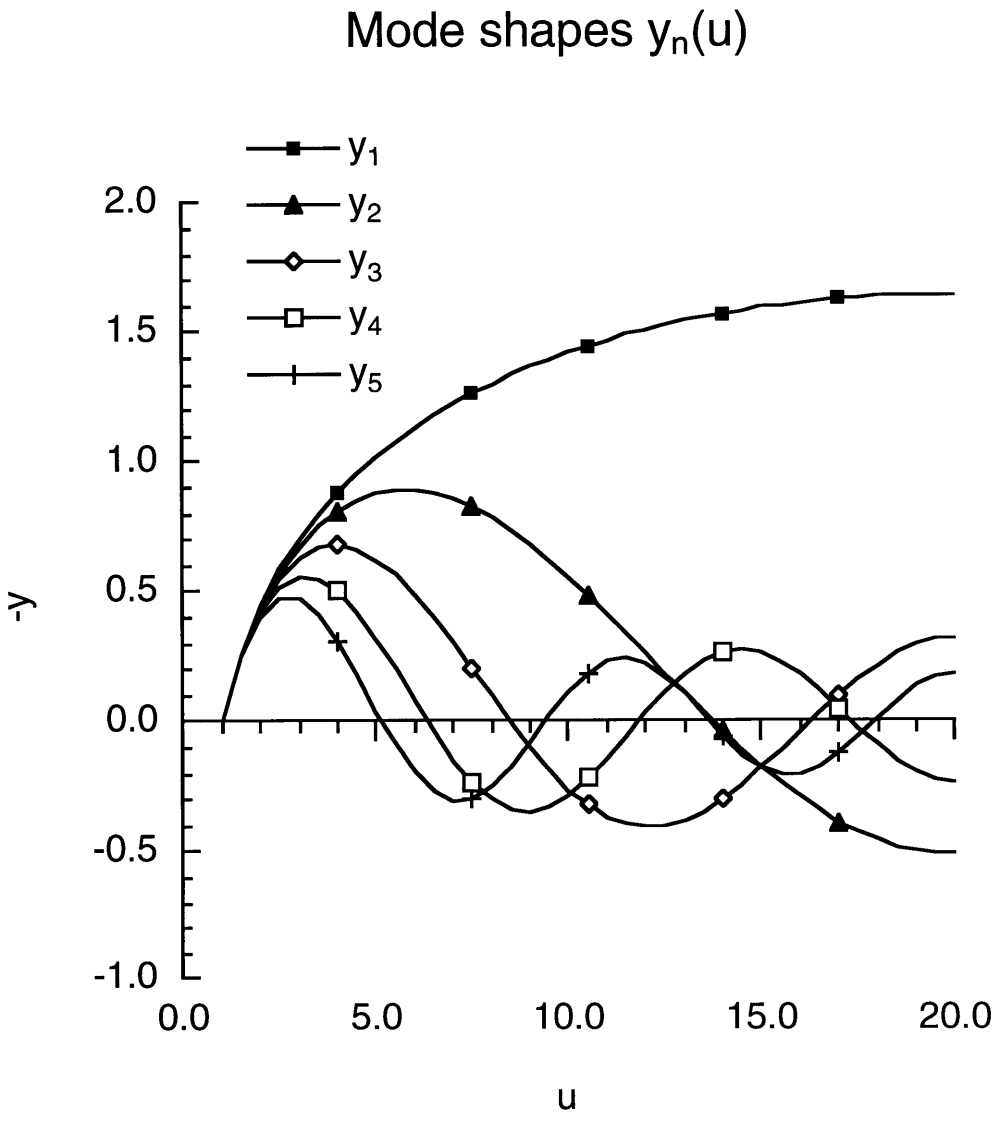

Figure 10. The first five mode shapes.

$$\theta(t) = exp(-d_0\lambda_n^2 g(t)) \tag{4-27}$$

Applying $R(r) = 1$ for $r_p \le r \le r_a$ at $t = 0$ to Eq. 4-20

$$1 = \sum_{n=1}^{\infty} C_n y_n(r), \quad r_p \le r \le r_a \tag{4-28}$$

Since $y_n(r)$ are orthogonal functions from the Sturm-Liouville Theorem [16], the constants C_n can be found by

$$C_n = \frac{\int_{r_p}^{r_a} r y_n(r) dr}{\int_{r_p}^{r_a} r y_n^2(r) dr} \tag{4-29}$$

Therefore, the complete solution is

$$\frac{c(r,t)}{c_0} = \sum_{n=1}^{\infty} C_n y_n \, exp(-d_0\lambda_n^2 g(t)) \tag{4-30}$$

Figure 11 shows a three mode approximation to Eq. 4-28. The first mode shape is seen to be dominant.

Let s be the total moisture concentration per unit length in the control volume, and apply $\alpha = r_a \,/\, r_p$ from Eq. 4-18

$$s = c_0 \sum_{n=1}^{\infty} C_n \, exp(-d_0\lambda_n^2 g(t)) \int_{r_p}^{\alpha r_p} y_n(r) 2\pi r \, dr \tag{4-31}$$

The initial total moisture concentration per unit length in the control volume is

$$s_0 = c_0\pi(\alpha^2 r_p^2 - r_p^2) = c_0\pi(\alpha^2 - 1)r_p^2 \tag{4-32}$$

The degree of conversion C_w equals the mass of moisture inside the control volume divided by the initial mass of moisture inside the control volume. So

$$C_w = \frac{s}{s_0} \tag{4-33}$$

Then the derivative of C_w with time equals the moisture release rate to the central pore channel. Let $u = r/r_p$ and transform the integral

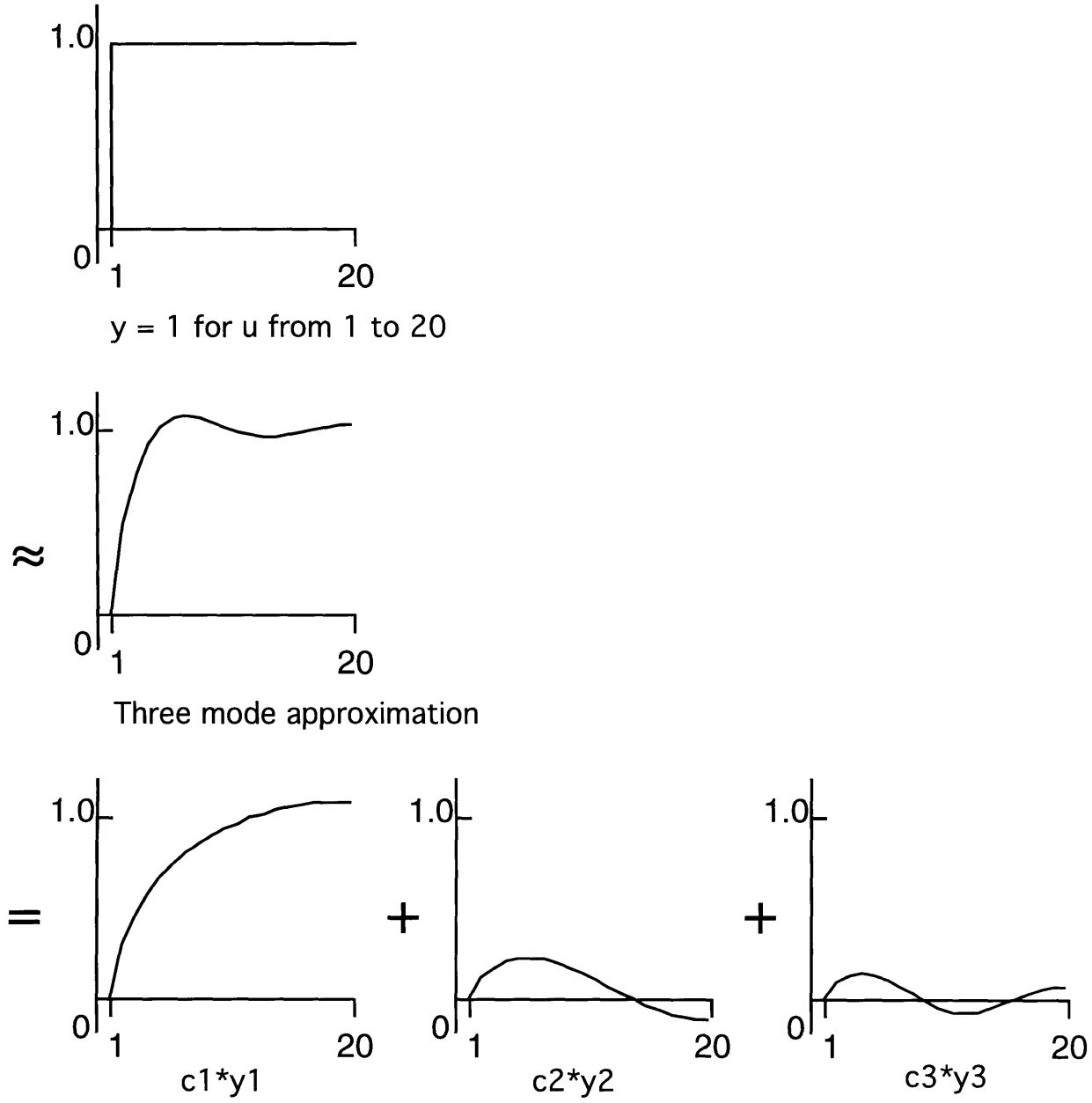

Figure 11. Three mode approximation.

$$\int_{r_p}^{\alpha r_p} y_n(r)\cdot 2\pi r dr = 2\pi r_p^2 \int_1^{\alpha} y_n(u)u\,du \tag{4-34}$$

where $$y_n(u) = Y_0(z_n)J_0(z_n u) - J_0(z_n)Y_0(z_n u) \tag{4-35}$$

Finally, combining Eqs. 4-29 through 4-35, the degree of conversion for zero moisture at the surface (moisture release in vacuum) is

$$C_u = \sum_{n=1}^{\infty} D_n \exp(-d_0 \lambda_n^2 g(t)) \tag{4-36}$$

where $$D_n = \frac{2}{\alpha^2 - 1} C_n \int_1^{\alpha} y_n(u)u\,du = \frac{2}{\alpha^2 - 1} \frac{(\int_1^{\alpha} y_n(u)u\,du)^2}{\int_1^{\alpha} y_n^2(u)u\,du} \tag{4-37}$$

Various values of z_n and D_n vs. α were calculated by Maple V (a general purpose mathematical software package similar to Mathematica) and are shown in Table 1 and 2. The radius ratio α can be found by the following approximation

$$\alpha = \sqrt{\frac{1}{nr_p^2}} \tag{4-38}$$

where n is the number of pore channels per unit area.

As seen in Table 1, higher mode shapes have larger z_n (and hence larger λ_n) so they decay faster. Also the difference between z_2 and z_1 is significantly larger than the difference between other z_{i+1} and z_i. As α increases, the z_n's decrease because more time is needed to diffuse a larger volume of moisture into the same pore channel. Table 2 shows that D_1 is relatively larger than other D_n's. The reason is clearly shown in Figure 12, where the volume of the first mode shape can be seen to be much larger than the others. If the radius ratio α is large, the series solution using only one mode will give good results. However, we used five modes to calculate the series solution more accurately since α in some cases was small.

Table 1. z_n **vs.** α

α	z_1	z_2	z_3	z_4	z_5
2	1.360777	4.645900	7.814163	10.967143	14.115058
5	0.282358	1.139215	1.939182	2.731206	3.520405
10	0.110269	0.497884	0.855429	1.208680	1.560290
20	0.046508	0.231750	0.401603	0.569335	0.736222
40	0.020448	0.111032	0.193820	0.275607	0.356993
50	0.015789	0.087928	0.153807	0.218902	0.283685
100	0.007166	0.042900	0.075464	0.107663	0.139720

Table 2. D_n **vs.** α

α	D_1	D_2	D_3	D_4	D_5
2	0.8702169	0.0629916	0.0219908	0.0111255	0.0067069
5	0.9307891	0.0350609	0.0115012	0.0057014	0.0034057
10	0.9583323	0.0222045	0.0067991	0.0032722	0.0019239
20	0.9743841	0.0144876	0.0041089	0.0019003	0.0010901
40	0.9835210	0.0098767	0.0026037	0.0011537	0.0006426
50	0.9855403	0.0088156	0.0022742	0.0009943	0.0005485
100	0.9900237	0.0063702	0.0015471	0.0006510	0.0003491

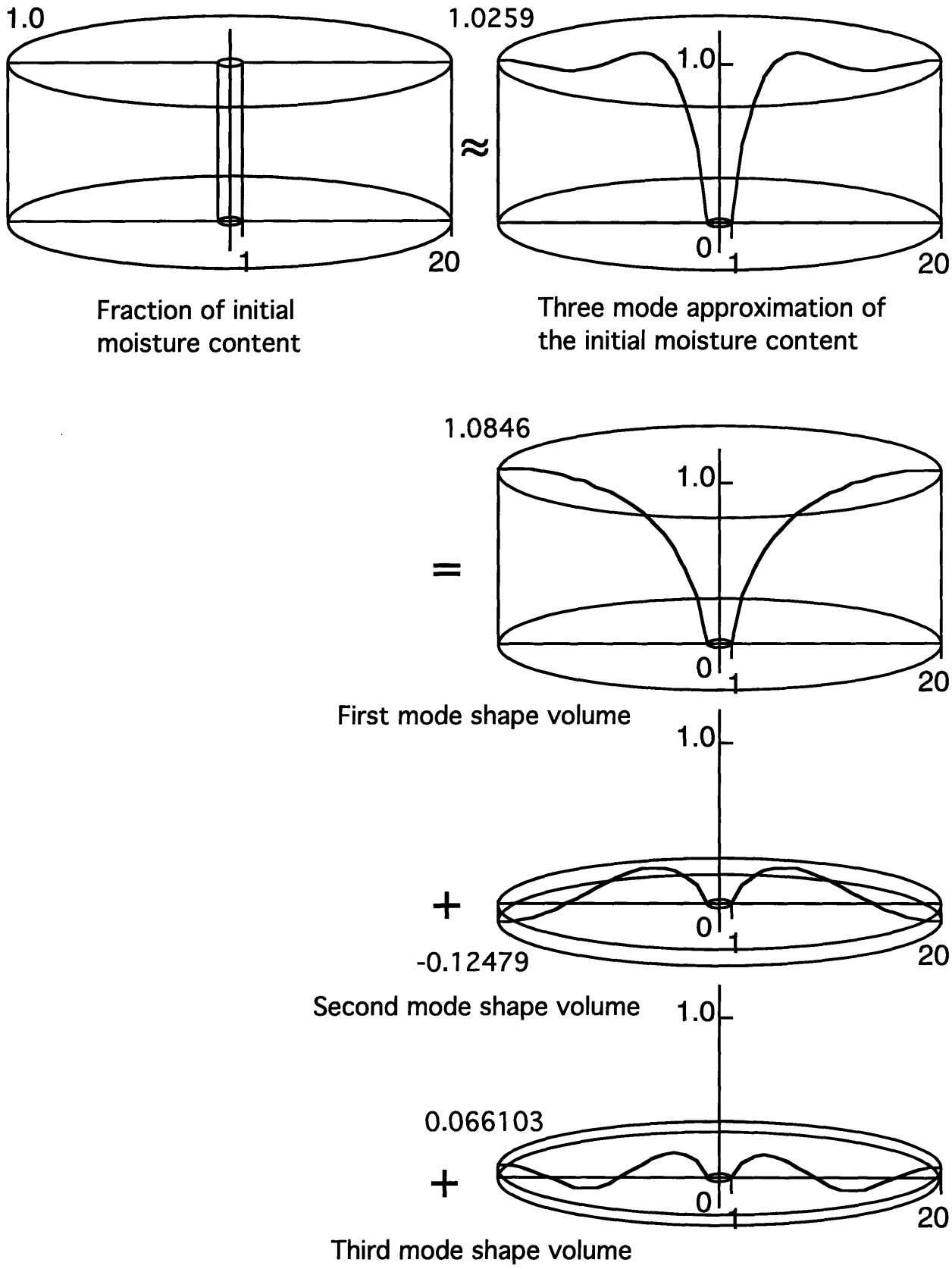

Figure 12. Three mode shape volume approximation.

If we put the initial condition of C_u into Eq. 4-36, then

$$C_u(0) = 1 = \sum_{n=1}^{\infty} D_n \tag{4-39}$$

However, since we truncate the series to five terms, we normalize the D_n so that the sum of five terms of D_n equals to 1 to satisfy the initial condition.

4.3 Equilibrium moisture concentration at surface

In general, the boundary condition at $r = r_p$ will not be zero. So we use the equilibrium moisture concentration to determine a new boundary condition. The equilibrium moisture concentration is given by the following empirical equation [15,17]

$$c_\infty = c_{max}\left(\frac{P_v}{P_{sat}(T)}\right)^b \tag{4-40}$$

where P_v is the vapor pressure of water, P_{sat} is the saturation pressure of water, and c_{max} is the maximum moisture content. If we assume that the moisture evaporation rate at the surface is very fast, then equilibrium is achieved at once at the surface. Thus, we have the new boundary condition

$$c(r_p) = c_\infty \tag{4-41}$$

Intuitively, the moisture concentration at the surface should be equal to the steam concentration in equilibrium, hence b should be close to 1. Since we lack the data for the carbon-phenolic composite materials, we let b equal 1 and c_{max} equal the maximum moisture content of 8% for the FM5055 composite material.

By convolution (see Appendix A for details), the degree of conversion is given by

$$\begin{aligned} C_w(t) &= f(t) - \int_0^t C_u(t-u)\frac{df}{dt}du \\ &= f(t) - \int_0^t \dot{f}(u)\sum_{n=1}^{\infty} D_n \exp(-d_0\lambda_n^2[g(t)-g(u)])du \end{aligned} \tag{4-42}$$

where the equilibrium degree of conversion $f(t) = c_\infty / c_0$ is given by

$$f(t) = \frac{c_{max}}{c_0}\left(\frac{P_v}{P_{sat}}\right)^b, \quad if\ P_v < P_{sat}$$
$$f(t) = \frac{c_{max}}{c_0}, \qquad if\ P_v \geq P_{sat} \tag{4-43}$$

Even though supersaturated steam may exists inside the pore channel (i.e. $P_v > P_{sat}(T)$), f cannot be greater than c_{max}/c_0 since the material could not physically absorb more moisture than the maximum amount. In that case, the supersaturated steam will probably condense to water inside the pore channels. This possible phenomena is neglected here so that a single phase flow of gas can be used. Furthermore, c_{max} is set equal to c_0 to prevent the computational difficulty of back moisture diffusion. In other words, f is restricted to be less than or equal to 1.

From Reynolds [18], the equation for the saturation pressure of water is determined by

$$ln\left(\frac{P_{sat}(T)}{P_c}\right) = \left(\frac{T_c}{T} - 1\right)\sum_{n=1}^{8} F_n\{a(T - T_p)\}^n \tag{4-44}$$

where T_c = 647.286K, P_c = 22.089 MPa, T_p = 338.15K, a = 0.01 and

F_1 = -7.4192420

F_2 = 2.9721000x10^{-1}

F_3 = -1.1552860x10^{-1}

F_4 = 8.6856350x10^{-3}

F_5 = 1.0940980x10^{-3}

F_6 = -4.3999300x10^{-3}

F_7 = 2.5206580x10^{-3}

F_8 = -5.2186840x10^{-4}

The plot of P_{sat} vs. T is shown in Figure 13.

The boundary function $f(T)$ is shown in Figure 14 for constant pressure P = 0.1, 1, 5 and 14 MPa respectively. f starts to decrease at the boiling temperature, where $P_{sat}(T)$ equals P. When the temperature rises above the critical temperature, f drops suddenly to zero.

The beta of moisture or degree of dry-out is

$$\beta_w = 1 - C_w \tag{4-45}$$

And the desired steam generation rate is

$$G_w = -c_0 \rho_s \frac{dC_w}{dt} = c_0 \rho_s \frac{d\beta}{dt} \tag{4-46}$$

where c_0 is the initial moisture content.

In summary, the equilibrium moisture concentration determines how much moisture inside the matrix is available to evaporate, and the evaporation rate is determined by the rate of moisture diffusion inside the matrix.

4.4 Numerical method

The steam generation rate (Eq. 4-46) is calculated numerically by a routine embedded in the CHAR code. Temperature and pressure conditions are provided by CHAR at each time step. These determine the boundary condition Eqs. 4-43 and 4-44. The degree of conversion C_w is found by numerically integrating Eq. 4-42 using the same time step as the rest of the CHAR solution, and the change in degree of conversion from the previous time step provides the generation rate. Details of the numerical method are provide in Appendix A.

4.4.1 Verification

If temperature is constant and pressure is zero, Eq. 4-26 becomes

$$g(t) = exp(-\frac{E_w}{R_g T})t \tag{4-47}$$

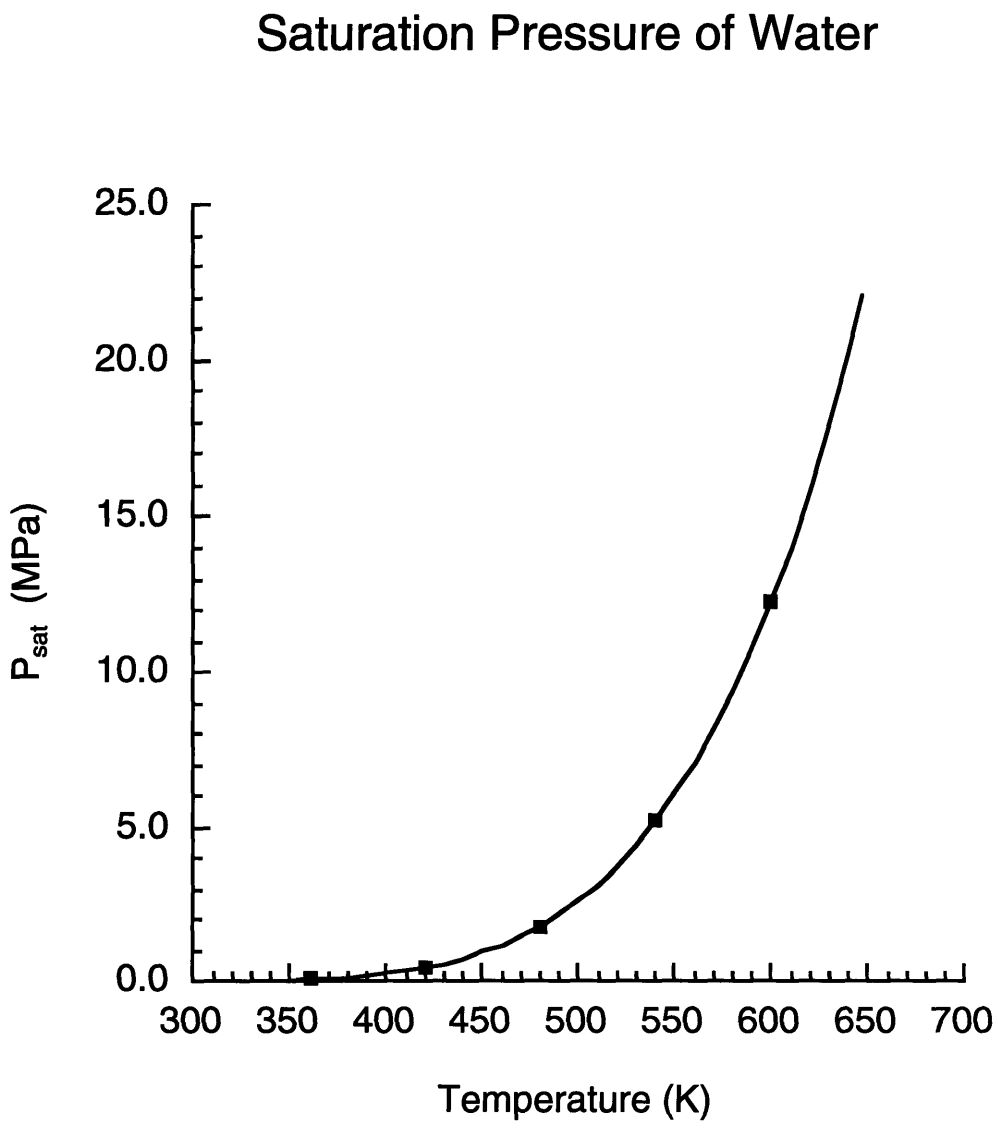

Figure 13. Saturation pressure of water.

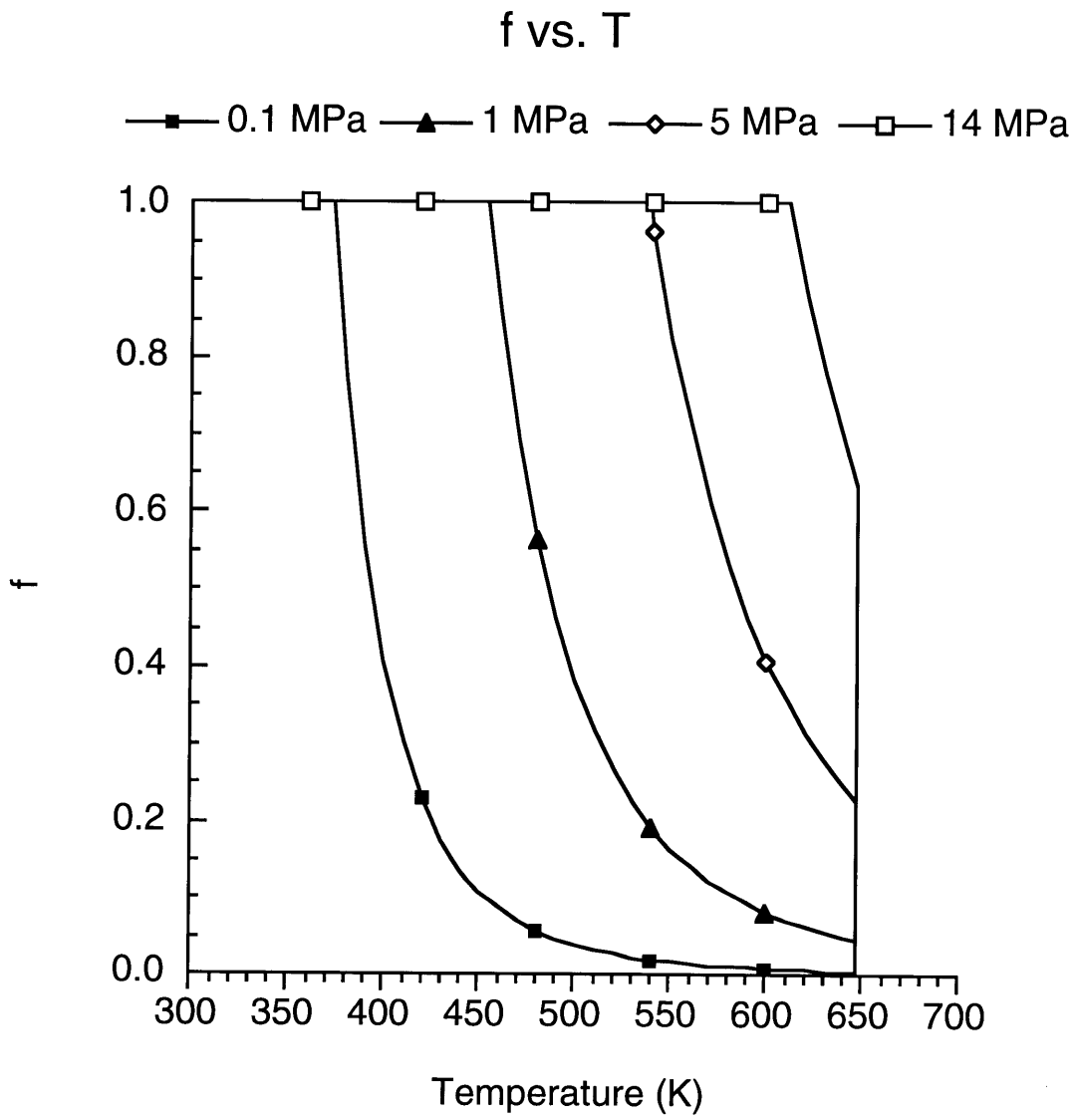

Figure 14. Equilibrium degree of conversion f for P = 0.1 MPa, 5 MPa, 14 MPa.

and the moisture content can be found from Eq. 4-36 directly. A small FORTRAN program was written to drive the CHAR subroutines for these simple cases. The results were compared with the exact solution of Eq. 4-36, and both results agreed with each other.

As an additional check, the solution from the CHAR subroutines was compared to the solution from the general purpose mathematical software Maple V for a constant pressure and temperature rise case. If $T = T_0 + ht$, where h is a constant temperature rise rate, then Eq. 4-26 becomes (see Appendix B for details)

$$g(t) = \frac{1}{h}\left(\frac{E_w}{R_g}\right)\left[p(x) - p(x_0)\right] \tag{4-48}$$

where

$$x = \frac{E_w}{R_g T}, \quad p(x) = \frac{exp(-x)}{x} + Ei(-x) \tag{4-49}$$

Ei(x) is the exponential function and the values of *-Ei(-x)* are tabulated in reference [19]. Equations 4-48 and 4-49 were used to express the integrand of Eq. 4-42 exactly, and Maple V performed the convolution integration. Figure 15 compares the Maple and CHAR subroutines solutions, and both solutions agree well.

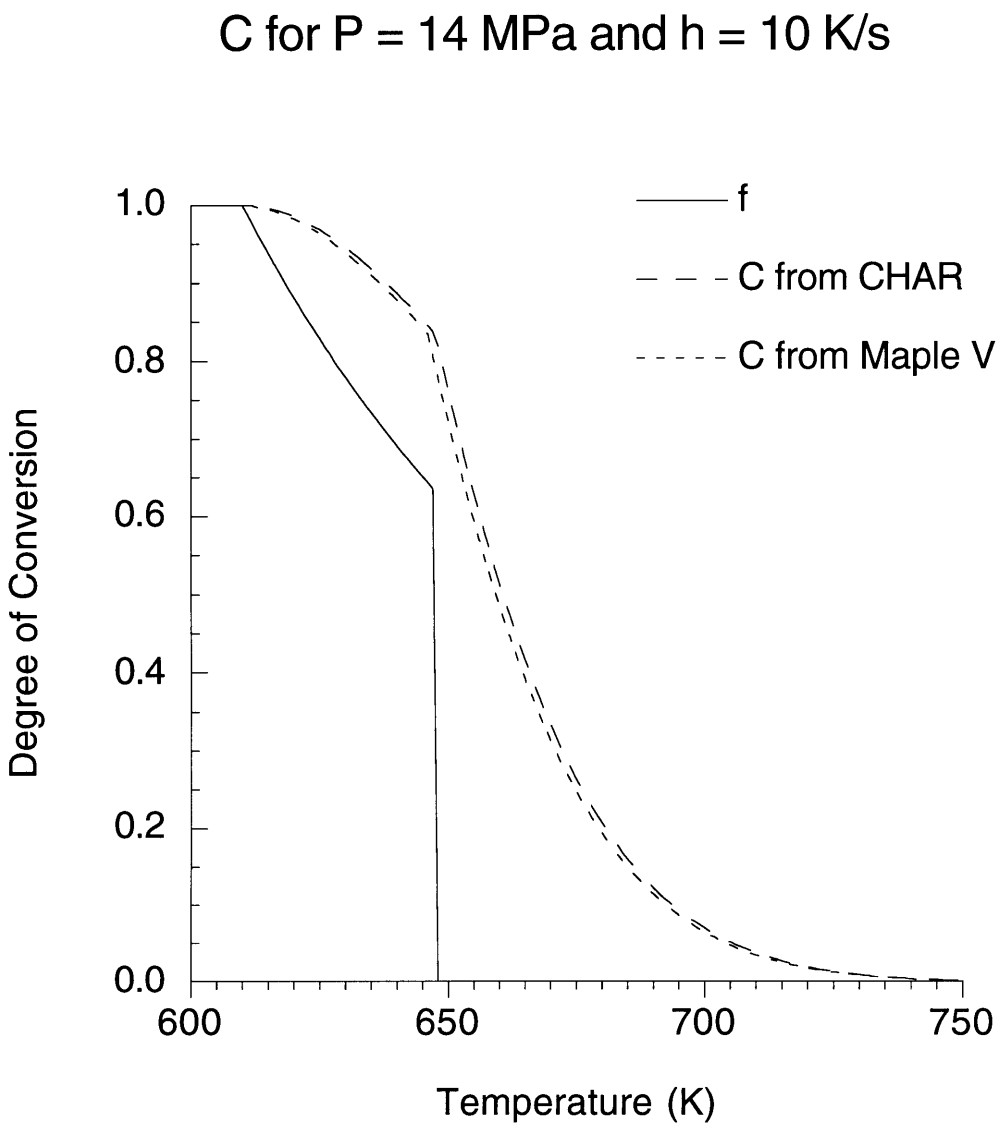

Figure 15. Numerical results.

5 Parametric Studies and Results

The new moisture release rate equation has been incorporated into the CHAR computer code using the numerical scheme in Appendix A. A standard case was established as a baseline for parametric studies. For FM5055, d_0 equals 0.118 mm²/s and E_w/R_g equals 4243K (across ply diffusion reported in [20]). Based on observed geometry [1], r_a equals 1 μm and r_p equals 20 μm. A CHAR model with 1001 nodes and 0.5 sec maximum time step was used to perform the studies. Despite the large number of nodes, typical run time on an IBM RS6000 320H workstation was 4 to 5 minutes. Parametric studies of various pore sizes, pore spacing, diffusivity constants, external pressures, and moisture contents, and comparisons to other models were performed.

5.1 Effects of pore size

According to Stokes [1], the diameter of closed crenulation channels is 1 to 3 μm. So we let r_p equal 4, 2, 1, and 0.5 μm and plot the maximum pressure difference histories in Figure 16. The maximum pressure difference is slightly higher for smaller pore sizes. History plots of C_w and f for r_p equal to 4, 2, 1, and 0.5 μm are shown in Figure 17. For larger r_p, the diffusion rate is faster so C_w follows f more closely. If the reaction rate is very fast, C_w can be approximated by f. This is the case for instant moisture release, and its pressure history plot is also shown in Figure 16. In all cases, the composite materials will not experience ply-life failure before shutoff.

Figure 18 and 19 show the propagation of pyrolysis and moisture evaporation zones, which are defined by the nodes within the range of $5\% < C < 95\%$, for the r_p equal 4 μm and instant release cases, respectively. The moisture evaporation reaction zone is smaller than the pyrolysis reaction zone. This is due to the fact that water has a higher boiling point at high pressure, so moisture evaporation will

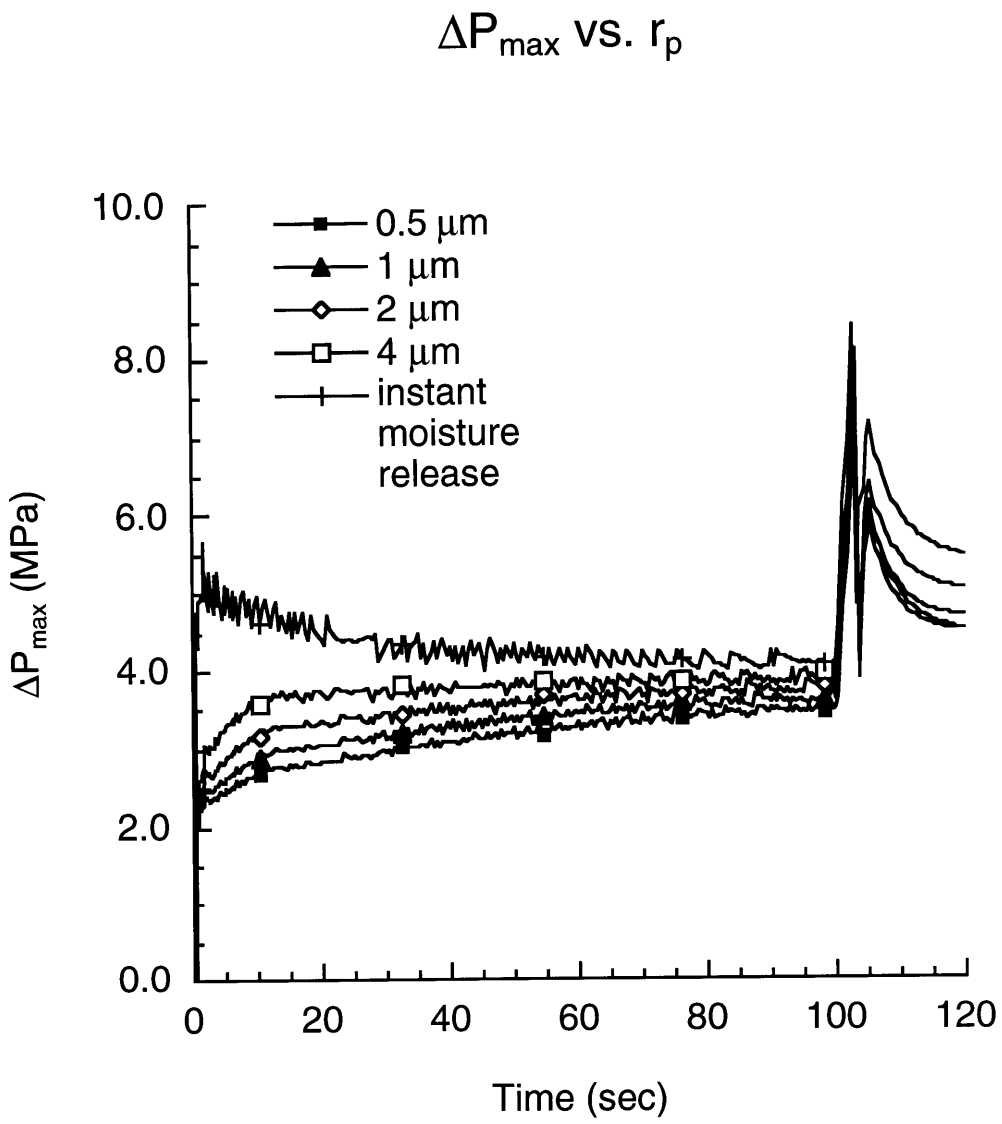

Figure 16. Maximum pressure difference vs. pore channel radius.

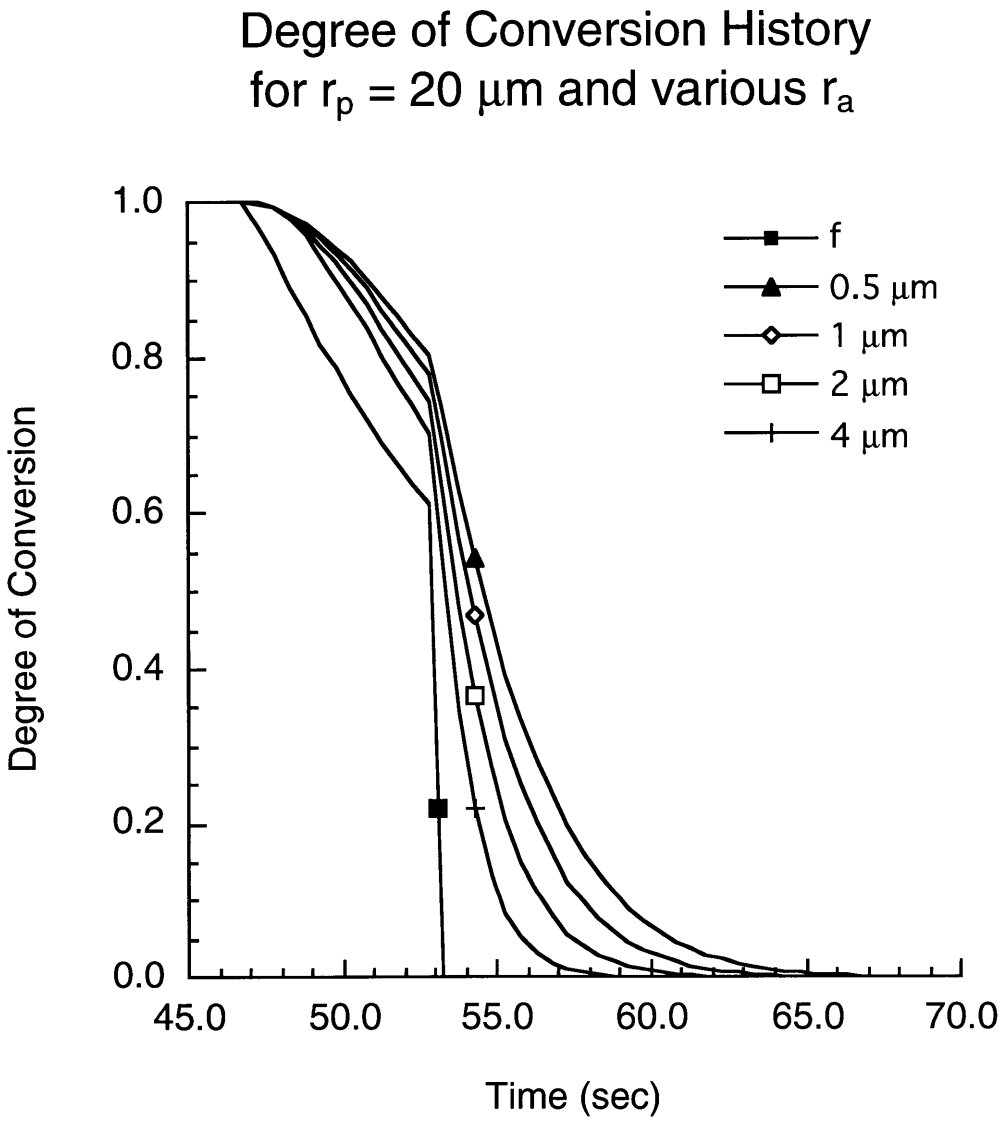

Figure 17. History plots of C and f.

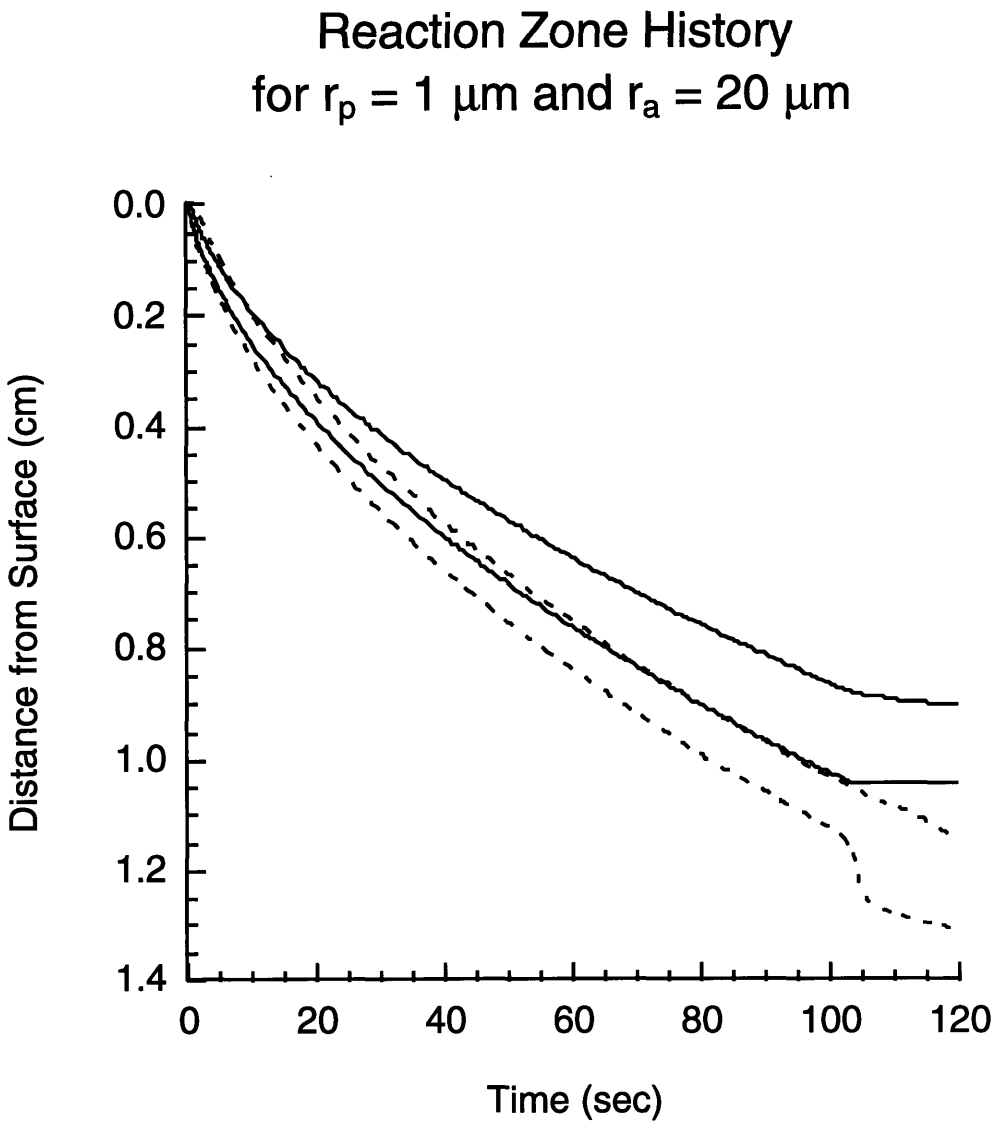

Figure 18. Reaction zone history for r_p = 1 μm and r_a = 20 μm. (Continuous lines represent the pyrolysis zone, and dashed lines represent the moisture evaporation zone)

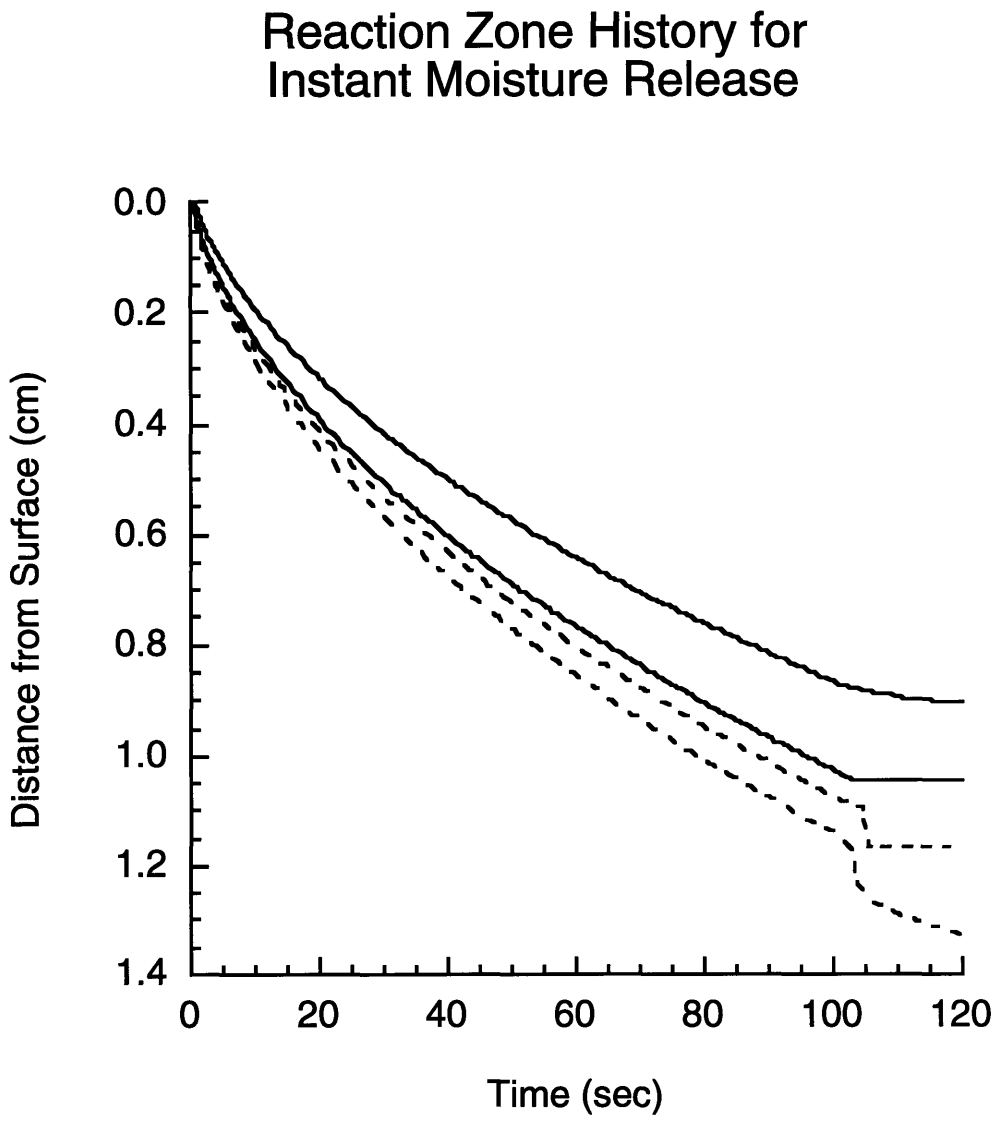

Figure 19. Reaction zone history for instant moisture release case. (Continuous lines represent pyrolysis zone, and dashed lines represents moisture evaporation zone)

not begin until the temperature passes the boiling point. Once the moisture begins to evaporate it will leave the material very fast due to high moisture diffusivity at high temperatures. After shut off, external pressure drops to 0.1 MPa and the moisture evaporation zone expands because more moisture is able to evaporate at lower pressure. The width of the gap between the two zones in the r_p equals 4 μm case is smaller than that in the instant moisture release case because the moisture escapes faster in the instant release rate case. The increase in gap distance results in a larger pressure gradient so the maximum pressure difference increases slightly.

5.2 Effects of pore spacing

As r_a increases, α increases such that all z_n decrease (see Table 1) and the moisture release takes a longer time to finish. As shown in Figure 20, the maximum pressure difference is notably lower for larger r_a. Figure 21 depicts the reaction zone histories which help to explain the reason for this lower maximum pressure difference. Since the moisture release takes longer to complete, the moisture evaporation zone becomes larger and does not separate from the pyrolysis zone. Because the permeability inside the pyrolysis zone is much greater than that of the virgin material, steam generated inside the pyrolysis zone can escape easily and causes a much smaller pressure rise.

5.3 Effects of diffusivity constants

The pre-exponential factor d_0 cannot be determined very accurately. For the same material, d_0 from different measurements can be different by as much as 2 orders of magnitude (from the reported data in Chapter 1 of [17]). So we vary the nominal d_0 by factors of ten times larger and smaller and plot the maximum pressure difference vs. time in Figure 22. The effect is similar to the result of varying r_a.

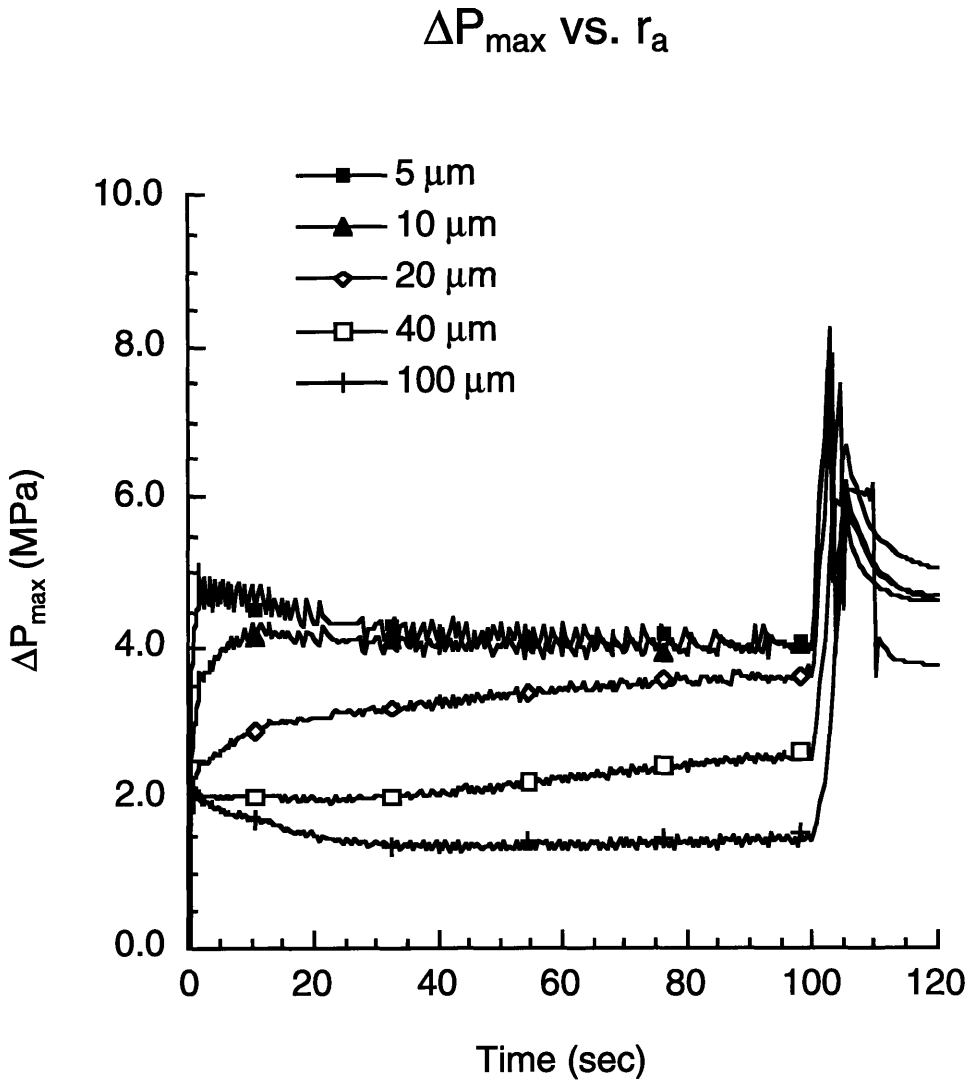

Figure 20. Maximum pressure difference vs. r_a.

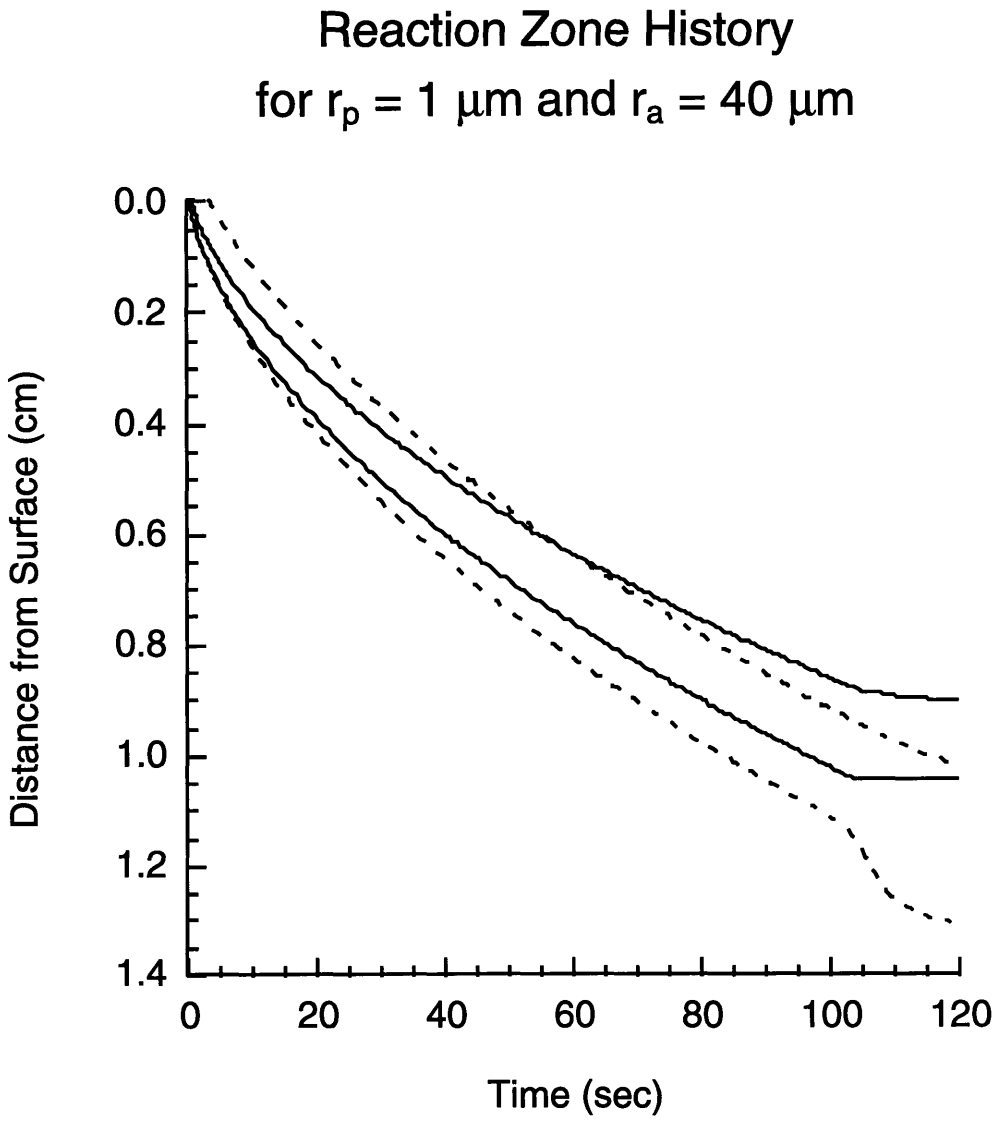

Figure 21. Reaction zone history for r_p = 1 μm and r_a = 40 μm. (Continuous lines represent pyrolysis zone, and dashed lines represents moisture evaporation zone)

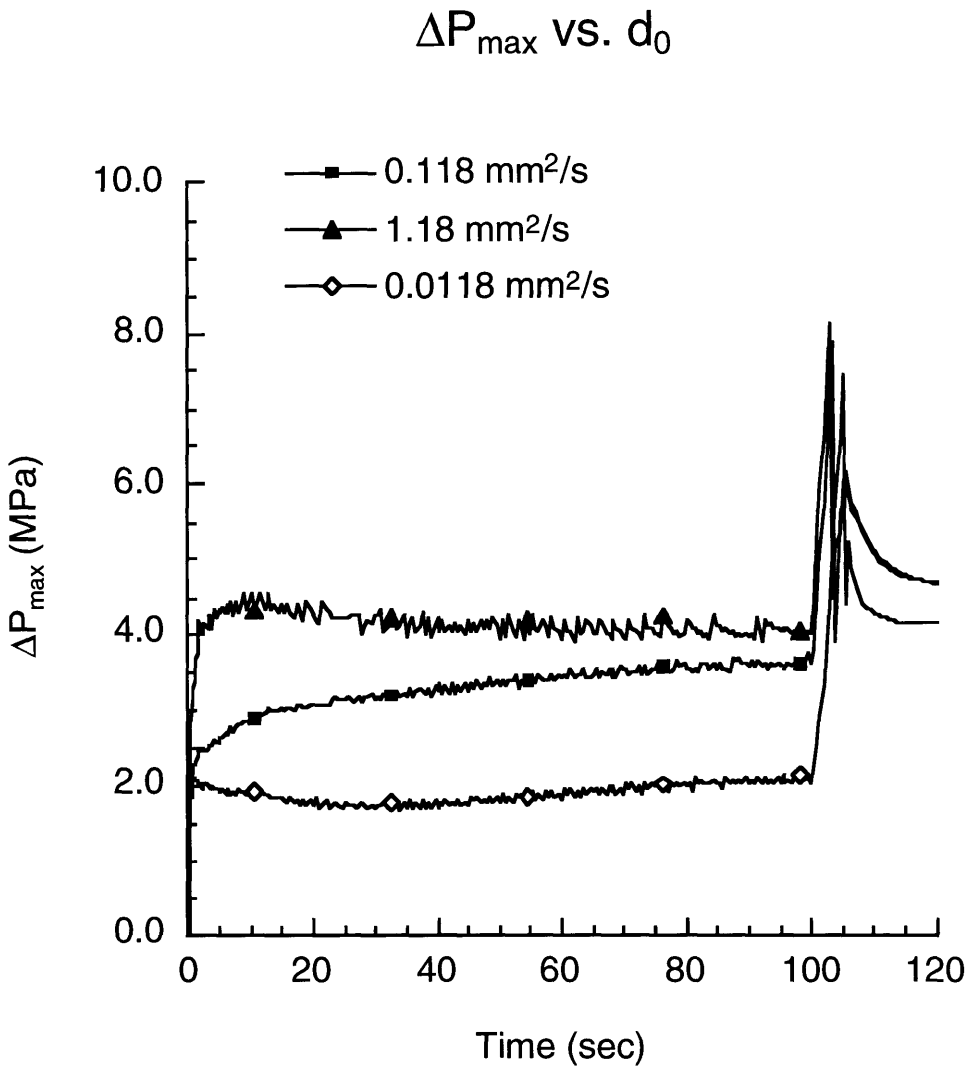

Figure 22. Maximum pressure difference vs. pre-exponent factor of moisture diffusion.

For E_w/R_g, the difference between with-ply and across-ply data from Stokes [20] is about 500 K. So we vary E_w/R_g by +500 K and -500 K. The corresponding maximum pressure difference is plotted in Figure 23. It shows a relatively small effect on the maximum pressure difference prediction.

5.4 Effects of external pressure

From Darcy's law (Eq. 2-6), mass flow is proportional to gas density ρ_g and pressure gradient dP/dz. Gas density is proportional to the average pressure and pressure gradient is proportional to the maximum pressure difference. Hence,

$$mf \propto P_{ave}\frac{\Delta P_{max}}{\Delta z} = \frac{(P_{max}+P_0)}{2\Delta z}(P_{max}-P_0) \propto P_{max}^2 - P_0^2 \tag{5-1}$$

Mass flow of gases is approximately proportional to the difference between the squares of maximum pressure and external pressure. Substituting $P_{max} = P_0 + \Delta P_{max}$, Eq. 5-1 becomes

$$mf \propto (\Delta P_{max}+P_0)^2 - P_0^2 = \Delta P_{max}^2 + 2\Delta P_{max}P_0 \tag{5-2}$$

From Eq. 5-2, for constant mass flow, it can be seen that the maximum pressure difference can be increased by decreasing external pressure. The sudden drop of external pressure after shut off causes the maximum pressure difference to rise and the composite materials to fail. This appears as a spike in many of the maximum pressure difference figures.

Furthermore, ply-lift can occur before shut off if the external pressure during service is low enough. Figure 24 depicts the maximum pressure difference with service external pressure P_0 equal 10, 5, 3.5, 3, and 0.1 MPa. As external pressure decreases, maximum pressure difference increases. For an external pressure equal to 3 MPa, the composite material experiences ply-lift before shut off. Ply-lift occurs where the maximum pressure difference is greater than about 6.2 MPa. Then, pressure drops suddenly and increases again. When the maximum pressure

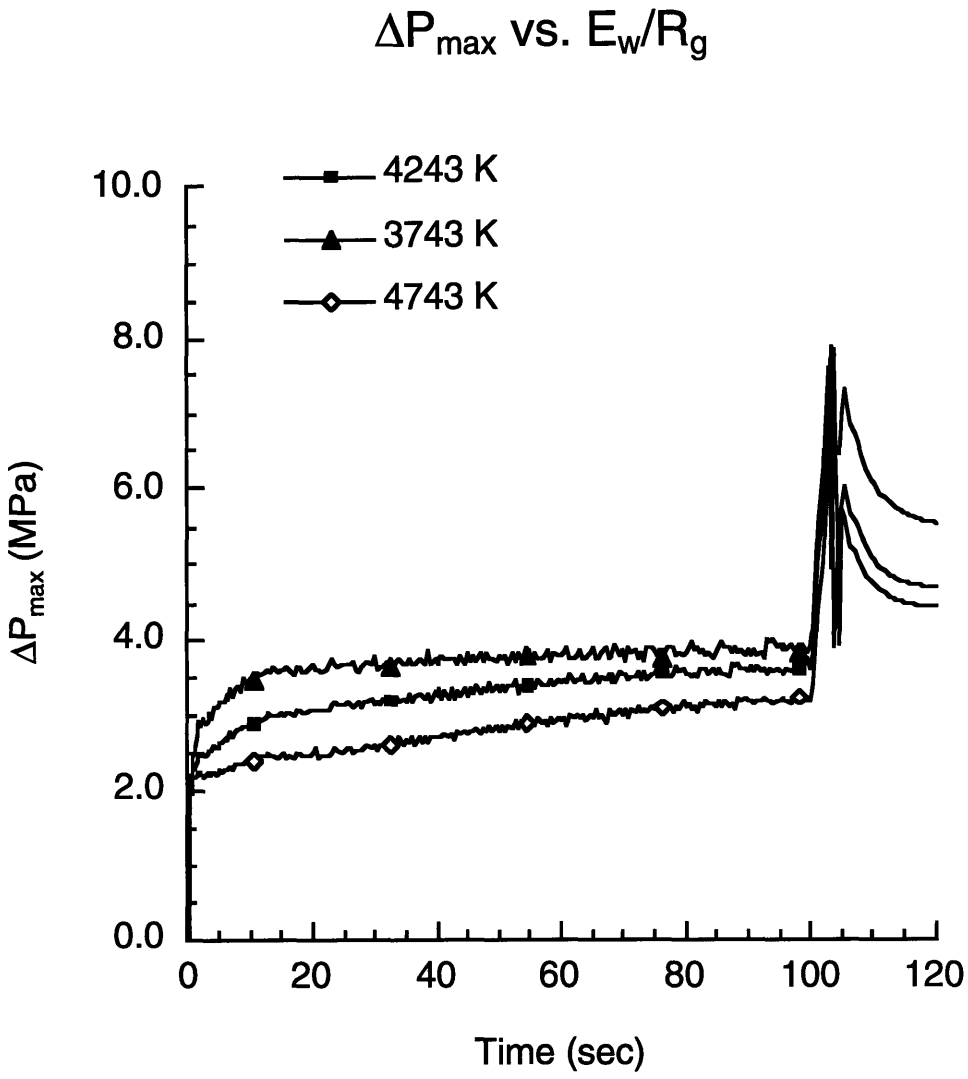

Figure 23. Maximum pressure difference vs. activation energy of moisture diffusion.

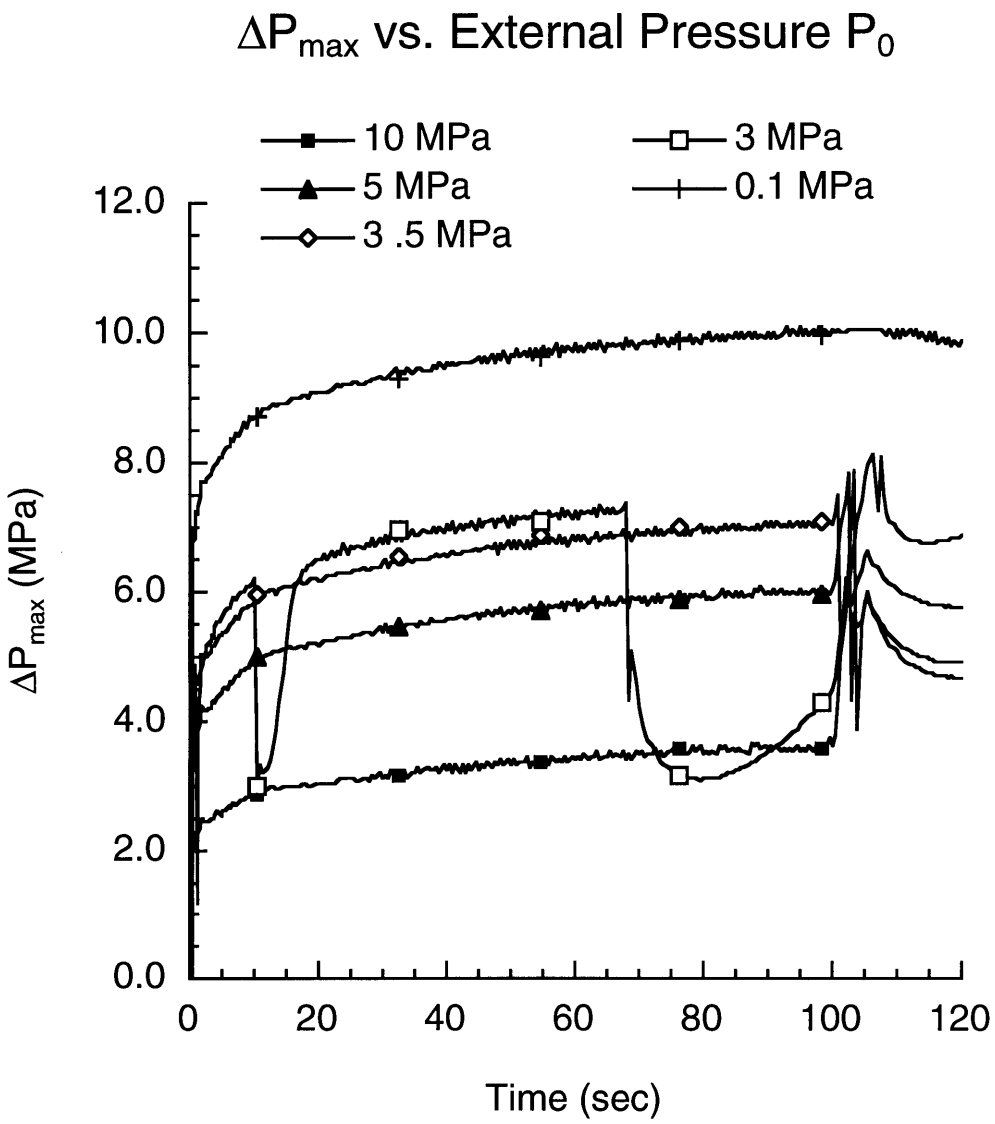

Figure 24. Maximum pressure difference vs. external pressure.

difference rises to about 7.3 MPa, the material fails again. For the case with an external pressure equal to 0.1 MPa, the material property input is altered such that no failure can occur. The result shows the maximum possible pressure difference inside a theoretical stronger material. The moisture evaporation zone for the case of an external pressure equal to 3.5 MPa is shown in Figure 25. It is larger than that in Figure 19, because at lower internal pressure, moisture can begin to evaporate or boil at a lower temperature.

5.5 Effects of initial and maximum moisture content

Figure 26 shows the maximum pressure difference calculated using several initial moisture contents: 0%, 1%, 3.5% (as-received), 5% and 8%. It shows that the maximum pressure difference increases as the initial moisture content increases. As expected, the internal pressure is very sensitive to initial moisture content. Even with the maximum moisture content of 8%, the materials will not fail in this case.

5.6 Comparisons to the other rate models

The new model was compared to the straight-line and Arrhenius models for moisture release. The original straight-line model used 50 K for ΔT. A ΔT of 100 K was also considered since this gave a much better match to the degree of conversion in Figure 15. The Arrhenius model was taken from a 4-part combined moisture release and pyrolysis model [3]. Only the first two parts, which are assumed to involve moisture release, were used.

Figure 27 shows the degree of conversion at a single node where the pressure is held constant at 0.1 MPa and the temperature increases linearly at 10 K/sec (typical in the later part of the simulation). Because the diffusivity is small at lower temperatures, the difference between degree of conversion with and without the boundary equation f is small. The Arrhenius model is reasonably matched to the

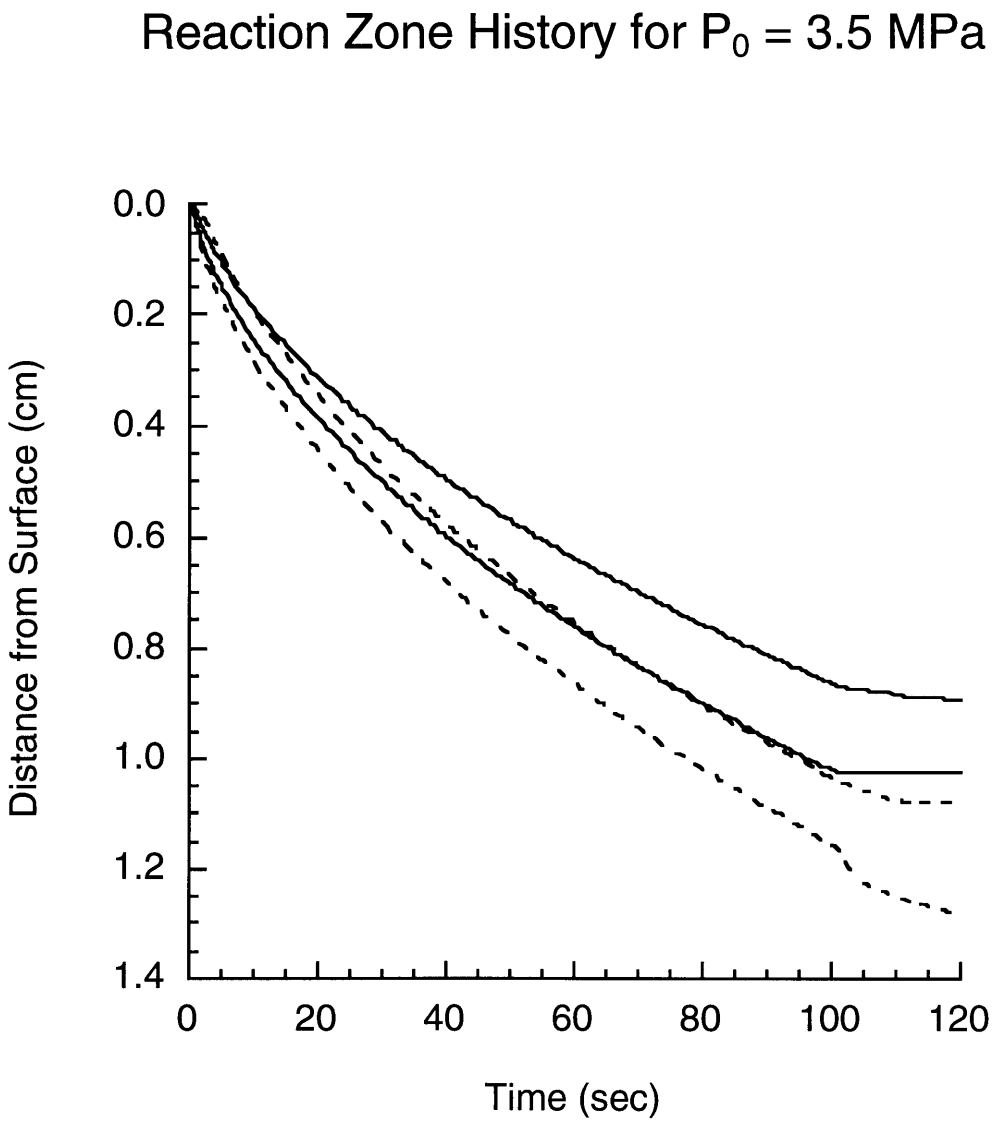

Figure 25. Reaction zone history for external pressure equals 3.5 MPa. (Continuous lines represent the pyrolysis zone, and dashed lines represent the moisture evaporation zone)

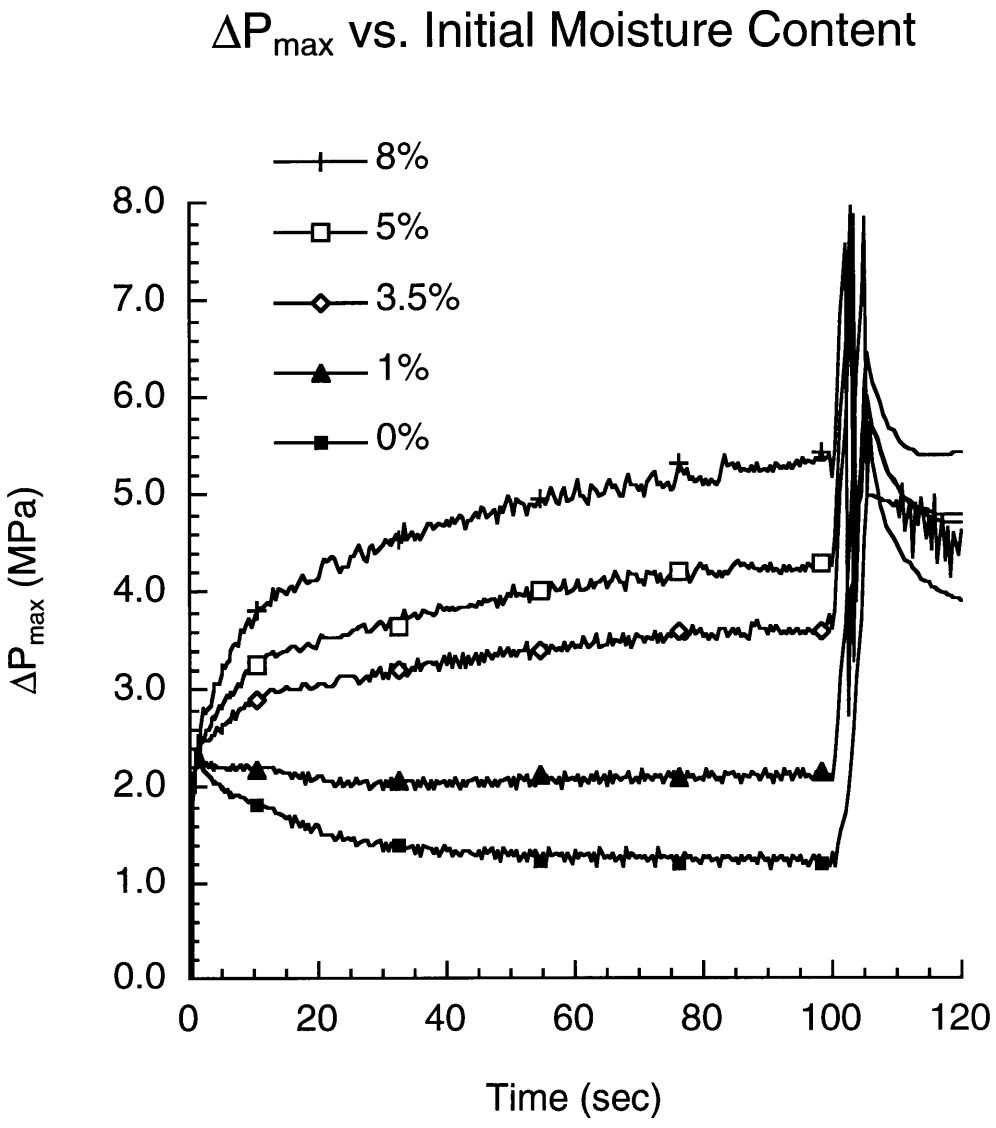

Figure 26. Maximum pressure difference vs. initial moisture content.

degree of conversion of the new model. The straight-line model gives much faster moisture release.

Figure 28 illustrates the degree of conversion for a constant pressure of 14 MPa. The heating rate for all cases except the one noted was 10 K/sec. As expected, the straight-line model for ΔT = 100 K is closed to the degree of conversion of the new model. However it is not close to the degree of conversion of the new model at heating rate of 30 K/sec (typical in the early part of the simulation).

Figure 29 shows the maximum pressure differences calculated with the new, straight-line, and Arrhenius models. The Arrhenius model overpredicts the maximum pressure difference because it is not pressure dependent. Although the degree of conversion for the Arrhenius model is close to the new model at low pressure in Figure 27, at high pressure it allows moisture release at temperatures below the saturation temperature of water. The straight-line model overpredicts the maximum pressure difference early in the simulation because it is not time dependent. A straight-line model, especially with ΔT = 100 K, gives good agreement at low temperature rise rates typical in the later part of the simulation. As can be seen from Figure 28, at high heating rates the straight-line model predicts faster moisture release. This results in a narrower moisture evaporation zone in Figure 30 than that in Figure 18 in the early part of the simulation, which in turn results in a higher maximum pressure difference. From Eq. 5-1, maximum pressure is proportional to the distance between the moisture evaporation zone and pyrolysis zone, and the amount of gases released. Although the distance between two zones increases with time in Figure 30, the maximum pressure difference decreases because the lower heating rate later in the simulation decreases the moisture release rate.

The maximum pressure difference prediction from the new model is bounded between the maximum pressure difference from zero moisture content (Figure 26)

and that from instant moisture release (Figure 16). This range is roughly shown in Figure 20. The moisture diffusion rate in the control volume determines the maximum pressure difference within this range.

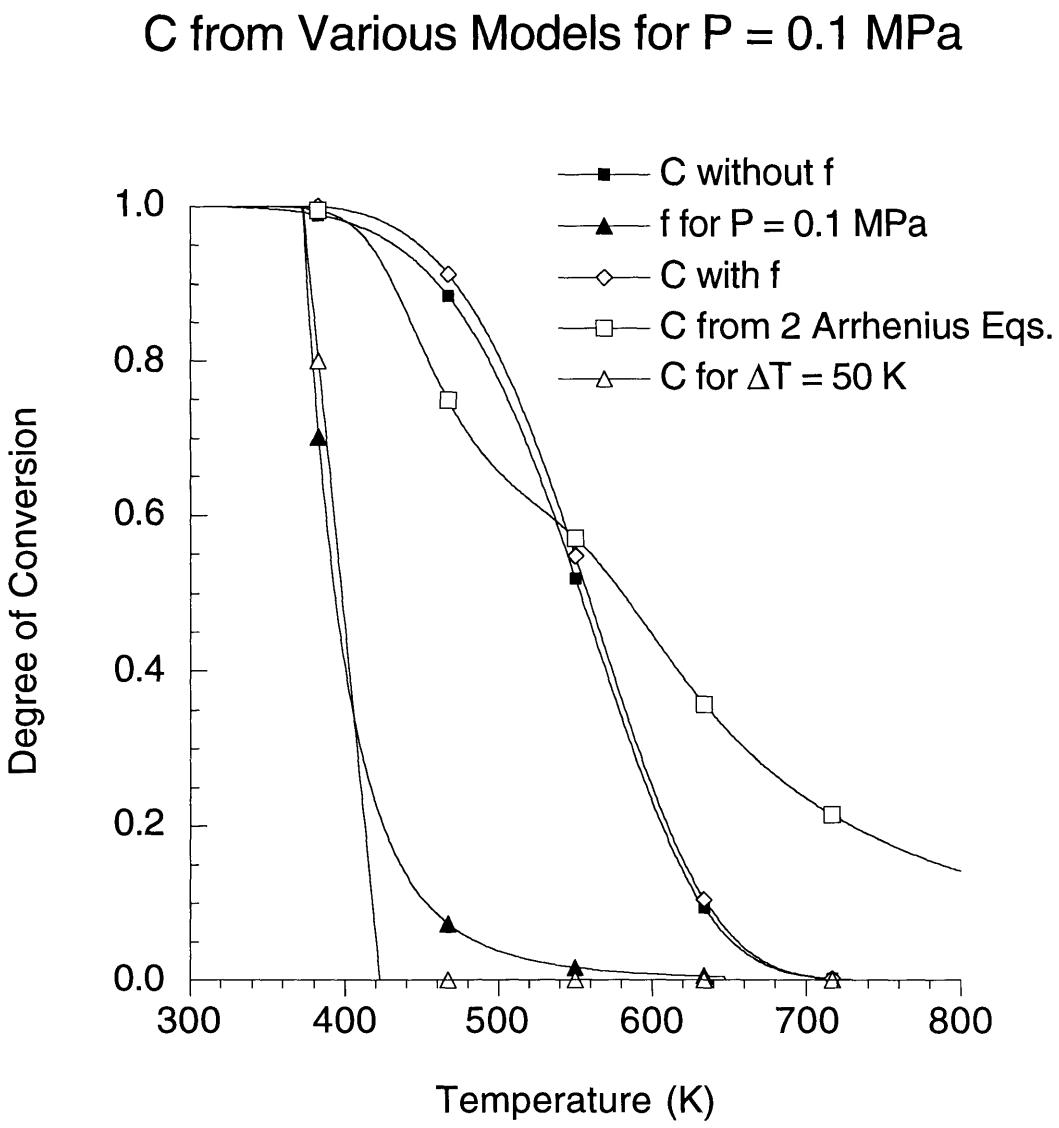

Figure 27. Degree of conversion from various models for P = 0.1 MPa and h = 10 K/s.

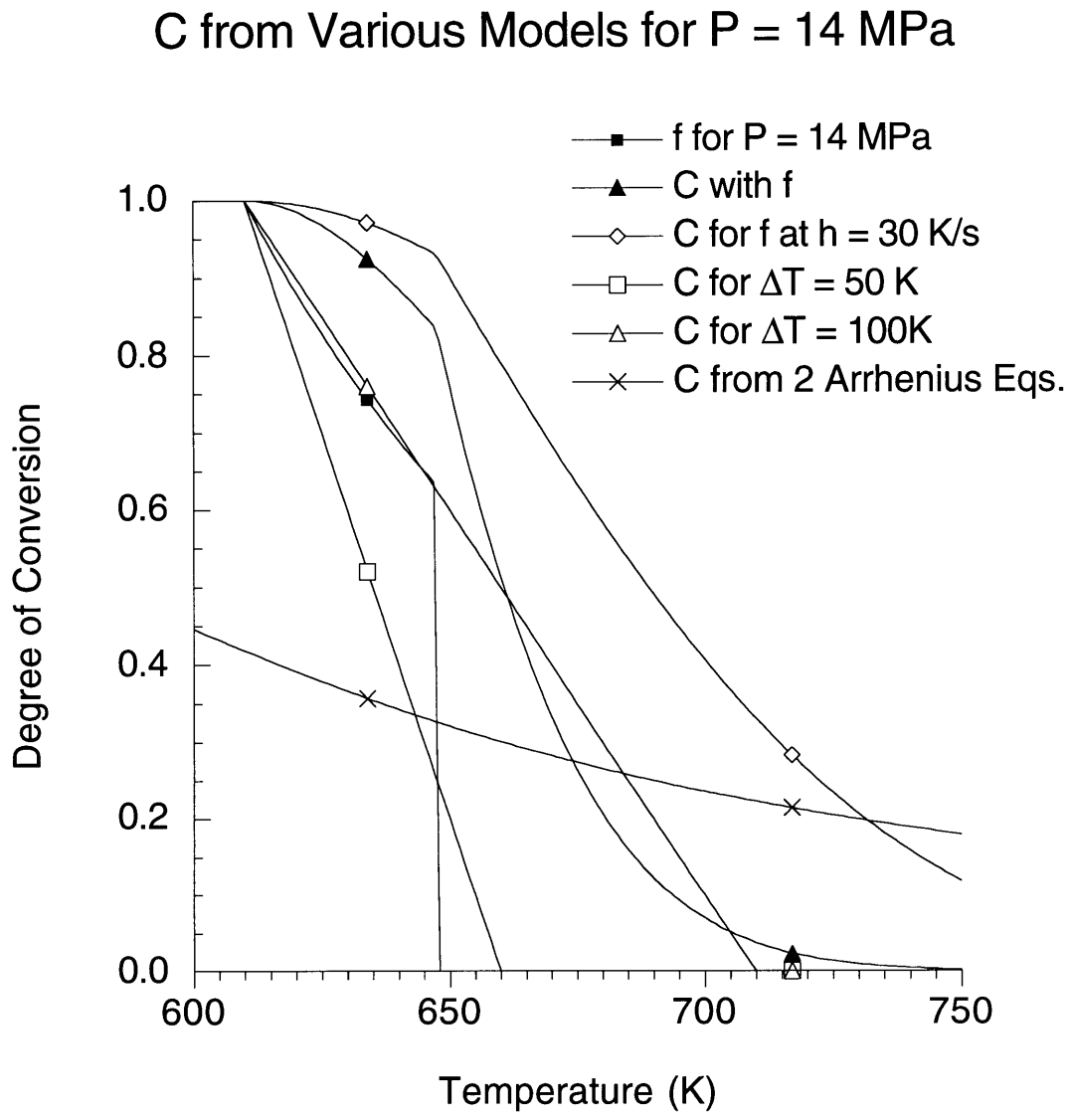

Figure 28. Degree of conversion from various models for P = 14 MPa and h = 10 K/s.

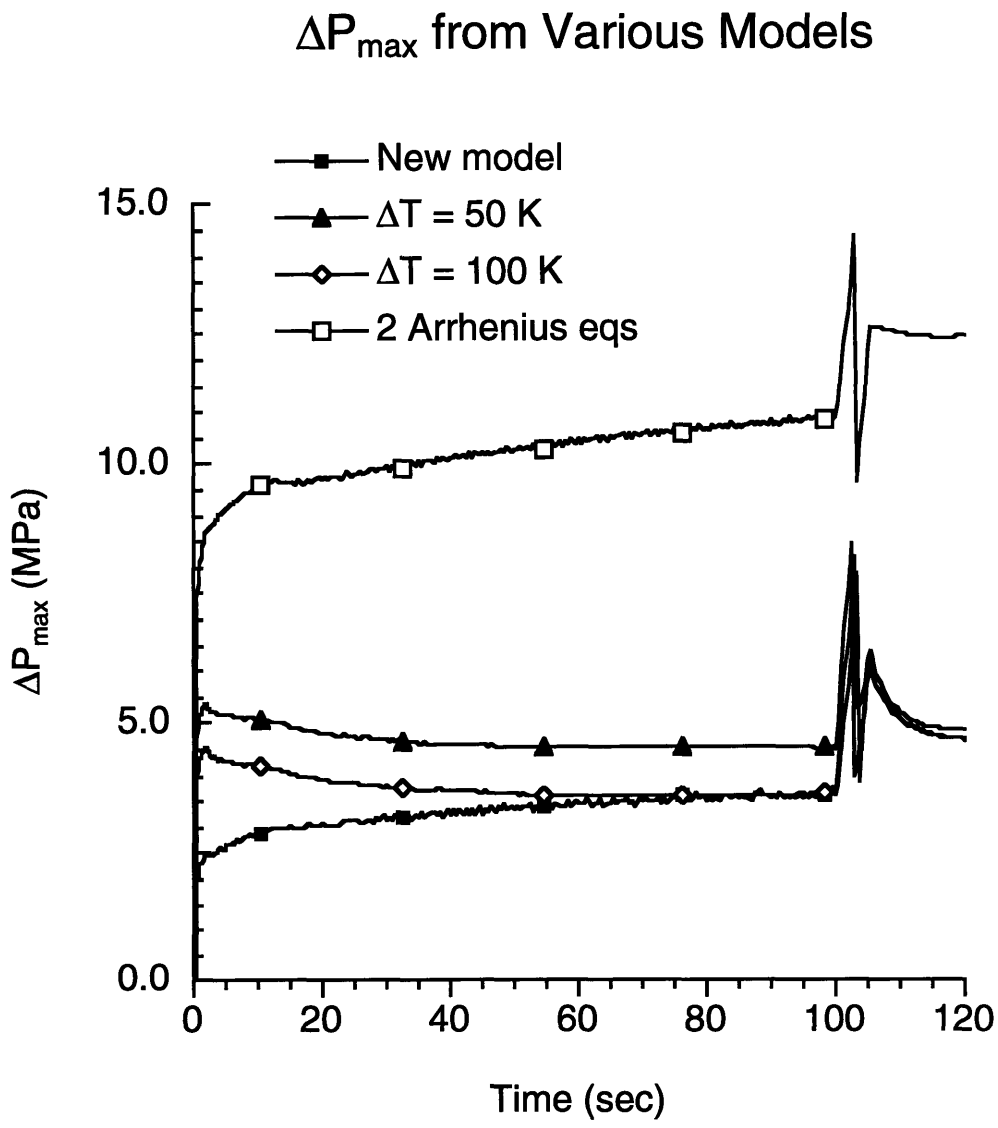

Figure 29. Maximum pressure difference from new, straight-line and Arrhenius models.

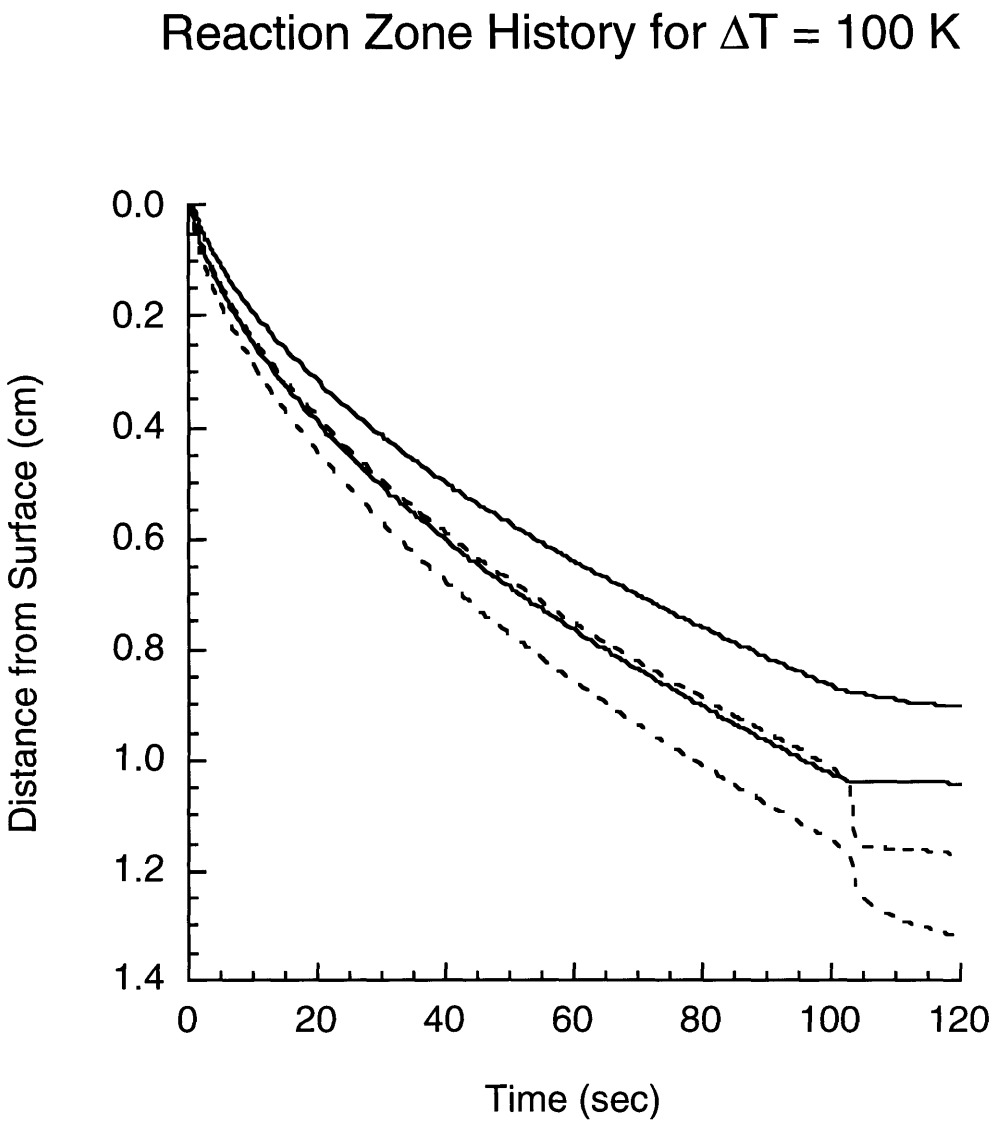

Figure 30. Reaction zone history for ΔT = 100 K. (Continuous lines represent the pyrolysis zone, and dashed lines represent the moisture evaporation zone)

6 Conclusions

The new method for calculating moisture release rates is based on a micro-scale model of moisture diffusion to a nearby pore channel and moisture evaporation on the pore channel surface. The diffusion of moisture causes the moisture release rate to be both time and temperature dependent. The equilibrium condition on the pore channel surface causes the moisture release rate to be dependent on pressure.

The method was expressed mathematically and implemented as a module of the CHAR code. It was found that only a few terms of the series solution were necessary for accurate results, resulting in good computational efficiency.

The inclusion of diffusion in the model slows the release of moisture. The delay of moisture release causes moisture to be released at higher temperature. This tends to remove the separation between the moisture evaporation and pyrolysis zones, and results in lower predicted pressures.

The geometry of the pores strongly effects the moisture release rate. Pore spacing has a larger effect than the pore size. Larger spacing (or smaller pore size) slows the diffusion to the pores and results in lower predicted pressure. Very large pore spacing slows the diffusion so much that the effect of moisture on predicted pressure is almost lost. Very small pore spacing allows very rapid moisture release to the limit that the diffusion effect is lost.

The value of the diffusivity rate constants have a lesser effect on the moisture release rate. Varying the values of the activation energy E_w well outside the measured range had only a moderate effect on the moisture release and pressure. Varying the rate constant d_0 by two orders of magnitude (also well outside the measured range) changed the calculated pressure difference by a factor of two.

The effects of external pressure and initial moisture content were also found to be very important. This result, known previously, was confirmed with the new model.

Because the new model is time, temperature, and pressure dependent, comparisons of the new model to existing Arrhenius and straight-line models illustrate how the more fundamental nature of the new model produces more physically realistic results under all conditions.

7 Recommendations

Future work should be done on:

1) Experiments to measure the rate of moisture release vs. temperature.
2) Experiments to measure the moisture diffusivity and material permeability at high temperatures.
3) Experiments to accurately measure the strength of the composite materials in the temperature range of ply-lift.
4) Modifications to the CHAR code to compare to RTG and CTE experimental results.

Also, the dependence of permeability on temperature, pressure and stress state [1] must be understood in order to gain further accuracy in predicting the internal pressure.

The new model could be modified to model the release rate of other absorbed substances such as carbon dioxide or chemi-absorbed water by the addition of a n-th order Arrhenius rate equation for the release rate of the substance from the material. This release rate will just be one more step in the schematic shown in Figure 9.

Appendix A Convolution of the new reaction rate equation and the numerical algorithm

In this appendix, we will find the solution for *C(t)* with an arbitrary boundary function *f(t)*, verify that solution by substitution into the corresponding differential equation, and outline the numerical implementation of the solution.

Notice that the old solution Eq. 4-36 is for a unit step down *f(t)* at $t = 0$. Also, $C_u(0) = 1$, $C_u(\infty) = 0$. Let

$$\begin{aligned} \beta_u(t) &= 1 - C_u(t) \\ q(t) &= 1 - f(t) \end{aligned} \tag{A-1}$$

Then the β_u is exact for an unit step function. If q varies by a small amount Δq in time τ, then

$$\beta(t) = \Delta q \beta_u(t - \tau) U(t - \tau) \tag{A-2}$$

where *U(t)* is unit step function($U(t) = 0$ for $t < 0$, $U(t) = 1$ for $t \geq 1$). If we model the response of continuous changes in q by a sum of all the small changes Δq, then

$$\begin{aligned} \beta(t) &= \int_0^t \beta_u(t-u) dq(u) \\ &= \int_0^t \beta_u(t-u) \dot{q}(u) du \end{aligned} \tag{A-3}$$

Transforming to *C(t)* by Eq. A-1,

$$\begin{aligned} C(t) &= 1 - \beta(t) \\ &= 1 - \int_0^t [1 - C_u(t-u)][-\dot{f}(u)] du \\ &= 1 + \int_0^t [1 - C_u(t-u)] \dot{f}(u) du \\ &= 1 + f(t) - f(0) - \int_0^t C_u(t-u) \dot{f}(u) du \\ &= f(t) - \int_0^t \dot{f}(u) \sum_{n=1}^{\infty} D_n \exp\left(-d_0 \lambda_n^2 \int_u^t \exp(-\frac{E_w}{R_g T(v)}) dv \right) du \\ &= f(t) - \int_0^t \dot{f}(u) \sum_{n=1}^{\infty} D_n \exp(-d_0 \lambda_n^2 [g(t) - g(u)]) du \end{aligned} \tag{A-4}$$

where *f(0)* = 1. Notice that in the convolution integral, we want

$$\int_u^t exp(-\frac{E_w}{R_g T(v)})dv = \int_0^t exp(-\frac{E_w}{R_g T(v)})dv - \int_0^u exp(-\frac{E_w}{R_g T(v)})dv = g(t) - g(u) \tag{A-5}$$

not the function g with the variable t - u directly.

$$g(t-u) = \int_0^{t-u} exp(-\frac{E_w}{R_g T(v)})dv \neq g(t) - g(u) \tag{A-6}$$

Now we prove the convolution solution satisfies the first order differential equation in time. First, we show the solution Eq. 4-27 for an unit step down $f(t)$ at $t = 0$

$$\theta(t) = exp\left(-d_0 \lambda_n^2 g(t)\right) = exp\left(-d_0 \lambda_n^2 \int_0^t exp(-\frac{E_w}{R_g T(v)})dv\right) \tag{A-7}$$

satisfies the first order differential equation Eq. 4-23

$$\frac{d\theta}{dt} = -d_0 \lambda_n^2 exp(-\frac{E_w}{R_g T(t)})\theta(t) \tag{A-8}$$

To prove it, use the differential formula for a definite integral from the CRC table [19]

$$\frac{d}{da}\left(\int_p^q f(x,a)dx\right) = \int_p^q \frac{\partial}{\partial a}[f(x,a)]dx + f(q,a)\frac{dq}{dt} - f(p,a)\frac{dp}{dt} \tag{A-9}$$

and differentiate Eq. A-7 with respect to time.

$$\begin{aligned} \frac{d\theta}{dt} &= \theta(t)\left[-d_0 \lambda_n^2 \left(exp(-\frac{E_w}{R_g T(t)}) - 0 - 0 \right)\right] \\ &= -d_0 \lambda_n^2 exp(-\frac{E_w}{R_g T(t)})\theta(t) \end{aligned} \tag{A-10}$$

Then the $C(t)$ for unit step down $f(t)$ is Eq. 4-36

$$C_u(t) = \sum_{n=1}^{\infty} D_n \theta(t) \tag{A-11}$$

The differential equation with boundary condition $f(t)$ is

$$\frac{d\theta}{dt} = -d_0\lambda_n^2 \exp(-\frac{E_w}{R_g T(t)})[\theta(t) - f(t)] \tag{A-12}$$

and the solution is the convolution of the previous $\theta(t)$ for unit step down $f(t)$

$$\theta(t) = f(t) - \int_0^t \exp\left(-d_0\lambda_n^2 \int_u^t \exp(-\frac{E_w}{R_g T(v)})dv\right)\dot{f}(u)du \tag{A-13}$$

To prove it, differentiate Eq. A-13 with respect to time.

$$\begin{aligned}
\frac{d\theta}{dt} &= \dot{f}(t) - \left\{\int_0^t \exp\left(-d_0\lambda_n^2 \int_u^t \exp(-\frac{E_w}{R_g T(v)})dv\right)\left[-d_0\lambda_n^2 \exp(-\frac{E_w}{R_g T(t)})\right]\dot{f}(u)du + \dot{f}(t)\right\} \\
&= \dot{f}(t) - \left\{[f(t) - \theta(t)]\left[-d_0\lambda_n^2 \exp(-\frac{E_w}{R_g T(t)})\right] + \dot{f}(t)\right\} \\
&= -d_0\lambda_n^2 \exp(-\frac{E_w}{R_g T(t)})[\theta(t) - f(t)]
\end{aligned} \tag{A-14}$$

Therefore, the full solution is

$$\begin{aligned}
C(t) &= \sum_{n=1}^{\infty} D_n \theta(t) \\
&= \sum_{n=1}^{\infty} D_n f(t) - \sum_{n=1}^{\infty} D_n \int_0^t \exp\left(-d_0\lambda_n^2 \int_u^t \exp(-\frac{E_w}{R_g T(v)})dv\right)\dot{f}(u)du \\
&= f(t) - \int_0^t \dot{f}(u) \sum_{n=1}^{\infty} D_n \exp\left(-d_0\lambda_n^2 \int_u^t \exp(-\frac{E_w}{R_g T(v)})dv\right)du
\end{aligned} \tag{A-15}$$

which confirms Eq. A-4.

The solution of A-4 can be found numerically by a finite difference in time method. We approximate the integral in Eq. A-4 as a sum of discrete time steps, truncate the summation on the modes, and note that

$$\dot{f}(t) \approx \frac{\Delta f(t)}{\Delta t} \tag{A-16}$$

For m modes and at time steps j ($t = j\Delta t$, where Δt is the time step), Eq. A-4 becomes

$$C(j\Delta t) = f(j\Delta t) - \sum_{i=0}^{j} \Delta f(i\Delta t) \sum_{n=1}^{m} D_n \exp\left(-d_0 \lambda_n^2 [g(j\Delta t) - g(i\Delta t)]\right) \tag{A-17}$$

Note that

$$\begin{aligned} g(j\Delta t) - g(i\Delta t) &= \int_0^{j\Delta t} \exp(-\frac{E_w}{R_g T(v)})dv - \int_0^{i\Delta t} \exp(-\frac{E_w}{R_g T(v)})dv \\ &= \int_{i\Delta t}^{j\Delta t} \exp(-\frac{E_w}{R_g T(v)})dv \end{aligned} \tag{A-18}$$

and switch the order of summation

$$C(j\Delta t) = f(j\Delta t) - \sum_{n=1}^{m} D_n \sum_{i=0}^{j} \Delta f(i\Delta t) \exp\left(-d_0 \lambda_n^2 \int_{i\Delta t}^{j\Delta t} \exp(-\frac{E_w}{R_g T(v)})dv \right) \tag{A-19}$$

Let $E_{n,j}$ be the part inside the summation of modes.

$$E_{n,j} = D_n \sum_{i=0}^{j} \Delta f(i\Delta t) \exp\left(-d_0 \lambda_n^2 \int_{i\Delta t}^{j\Delta t} \exp(-\frac{E_w}{R_g T(v)})dv \right) \tag{A-20}$$

Then Eq. A-19 becomes

$$C(j\Delta t) = f(j\Delta t) - \sum_{n=1}^{m} E_{n,j} \tag{A-21}$$

At the next time step $j+1$, $E_{n,j+1}$ becomes

$$\begin{aligned} E_{n,j+1} &= D_n \sum_{i=0}^{j+1} \Delta f(i\Delta t) \exp\left(-d_0 \lambda_n^2 \int_{i\Delta t}^{(j+1)\Delta t} \exp(-\frac{E_w}{R_g T(v)})dv \right) \\ &= D_n \sum_{i=0}^{j} \Delta f(i\Delta t) \exp\left(-d_0 \lambda_n^2 \int_{i\Delta t}^{(j+1)\Delta t} \exp(-\frac{E_w}{R_g T(v)})dv \right) + D_n \Delta f\big((j+1)\Delta t\big) \\ &= D_n \sum_{i=0}^{j} \Delta f(i\Delta t) \exp\left(-d_0 \lambda_n^2 \left\{ \int_{i\Delta t}^{j\Delta t} \exp(-\frac{E_w}{R_g T(v)})dv + \int_{j\Delta t}^{(j+1)\Delta t} \exp(-\frac{E_w}{R_g T(v)})dv \right\} \right) \\ &\quad + D_n \Delta f\big((j+1)\Delta t\big) \\ &= D_n \exp\left(-d_0 \lambda_n^2 \int_{j\Delta t}^{(j+1)\Delta t} \exp(-\frac{E_w}{R_g T(v)})dv \right) \sum_{i=0}^{j} \Delta f(i\Delta t) \exp\left(-d_0 \lambda_n^2 \int_{i\Delta t}^{j\Delta t} \exp(-\frac{E_w}{R_g T(v)})dv \right) \\ &\quad + D_n \Delta f\big((j+1)\Delta t\big) \end{aligned} \tag{A-22}$$

In terms of the value at the previous time step, we get an iterative equation for $E_{n,j+1}$

$$E_{n,j+1} = E_{n,j}\, exp\left(-d_0\lambda_n^2 \int_{j\Delta t}^{(j+1)\Delta t} exp(-\frac{E_w}{R_g T(v)})dv \right) + D_n \Delta f((j+1)\Delta t) \tag{A-23}$$

The complete numerical scheme is

$$\begin{aligned}
&Initially, \quad f(0)=1, \quad E_{n,0}=0 \quad for\ all\ n \\
&\Delta f(j\Delta t) = f(j\Delta t) - f((j-1)\Delta t) \\
&E_{n,j} = E_{n,j-1}\, exp(-d_0\lambda_n^2 \Delta g_j) + D_n \Delta f(j\Delta t) \quad for\ all\ n \\
&C(j\Delta t) = f(j\Delta t) - \sum_{n=1}^{m} E_{n,j} \\
&where \quad \Delta g_j = \int_{(j-1)\Delta t}^{j\Delta t} exp(-\frac{E_w}{R_g T(v)})dv
\end{aligned} \tag{A-24}$$

The integral Δg_j can be calculated by 2 point (end point) approximation.

$$\Delta g_j = \frac{1}{2}\left(exp(-\frac{E_w}{R_g T_j}) + exp(-\frac{E_w}{R_g T_{j-1}}) \right)\Delta t \tag{A-25}$$

Since Eq. A-25 depends on the value of T at current time step j, the numerical solution Eq. A-24 is a mixed implicit-explicit scheme and hence more likely to be stable.

Notice that Δf in Eq. A-24 is modeled as a step change at time step j. A more accurate method is to modeled Δf as linear change from time step *j-1* to time step j. The numerical scheme is then

$$\begin{aligned}
&Initially, \quad f(0)=1, \quad E_{n,0}=0 \quad for\ all\ n \\
&\Delta f(j\Delta t) = f(j\Delta t) - f((j-1)\Delta t) \\
&\Delta g_j = \frac{1}{2}\left(exp(-\frac{E_w}{R_g T_j}) + exp(-\frac{E_w}{R_g T_{j-1}}) \right)\Delta t \\
&E_{n,j} = \left(E_{n,j-1} + \frac{\Delta f(j\Delta t)}{d_0\lambda_n^2 \Delta g_j} D_n \right) exp(-d_0\lambda_n^2 \Delta g_j) - \frac{\Delta f(j\Delta t)}{d_0\lambda_n^2 \Delta g_j} D_n \quad for\ all\ n \\
&C(j\Delta t) = f(j\Delta t) - \sum_{n=1}^{m} E_{n,j}
\end{aligned} \tag{A-26}$$

This numerical scheme was used in the CHAR routines.

Appendix B Exact solution of the degree of conversion from the Arrhenius rate equation for a constant temperature rise case

The general n-th order Arrhenius rate equation is

$$\frac{dC}{dt} = -AC^n exp(-\frac{E_a}{R_g T(t)}) \tag{B-1}$$

At $t = 0$, $C = 1$ and at $t = \infty$, $C = 0$. Integrating both sides,

$$\int_1^{C(t_1)} \frac{1}{C^n} dC = -A\int_0^{t_1} exp(-\frac{E_a}{R_g T(t)})dt = -Ag(t_1) \tag{B-2}$$

where subscript 0 indicates the initial state, and subscript 1 indicates the current state.

For $n = 1$

$$\begin{aligned} &\int_1^{C(t_1)} \frac{1}{C} dC = ln(C(t_1)) - ln(0) = ln(C(t_1)) = -Ag(t_1) \\ &C(t_1) = exp(-Ag(t_1)) \end{aligned} \tag{B-3}$$

For $n \neq 1$

$$\begin{aligned} &\int_1^{C(t_1)} \frac{1}{C^n} dC = \frac{1}{-n+1} C^{-n+1}\Big|_1^{C(t_1)} = \frac{(C^{-n+1}(t_1) - 1)}{1-n} = -Ag(t_1) \\ &C(t_1) = \left[1 + (n-1)Ag(t_1)\right]^{\frac{1}{1-n}} \end{aligned} \tag{B-4}$$

Then,

$$C(t_1) = \begin{cases} exp(-Ag(t_1)) & for\ n = 1 \\ \left[1 + (n-1)Ag(t_1)\right]^{\frac{1}{1-n}} & for\ n \neq 1 \end{cases} \tag{B-5}$$

For the function $g(t_1)$,

$$g(t_1) = \int_0^{t_1} exp(-\frac{E_a}{R_g T(t)})dt \tag{B-6}$$

Let the temperature rise be a constant h,

$$T = T_0 + ht, \quad \frac{dT}{dt} = h \tag{B-7}$$

Then, change the variable time t into temperature T

$$g(T_1) = \frac{1}{h}\int_{T_0}^{T_1} exp(-\frac{E_a}{R_g T})dT \tag{B-8}$$

Let

$$x = \frac{E_a}{R_g T}, \quad T = \frac{E_a}{R_g x}, \quad dT = -\frac{E_a}{R_g x^2}dx \tag{B-9}$$

and change T into x

$$g(x_1) = \frac{1}{h}\int_{x_0}^{x_1} exp(-x)\left(-\frac{E_a}{R_g}\right)\frac{dx}{x^2} \tag{B-10}$$

Using integration by parts,

$$\begin{aligned} u &= exp(-x) & dv &= \frac{dx}{x^2} \\ du &= -exp(-x)dx & v &= -\frac{1}{x} \end{aligned} \tag{B-11}$$

Eq. B-10 becomes

$$g(x_1) = \frac{1}{h}\left(\frac{E_a}{R_g}\right)\left[\frac{exp(-x_1)}{x_1} - \frac{exp(-x_0)}{x_0} + \int_{x_0}^{x_1}\frac{exp(-x)}{x}dx\right] \tag{B-12}$$

Let

$$p(x) = \frac{exp(-x)}{x} - \int_x^{\infty}\frac{exp(-s)}{s}ds = \frac{exp(-x)}{x} - (-Ei(-x)) \tag{B-13}$$

where the exponential integral function $-Ei(-x)$ is tabulated in [19].

Then $g(x_1)$ becomes

$$g(x_1) = \frac{1}{h}\left(\frac{E_a}{R_g}\right)\left[p(x_1) - p(x_0)\right] \tag{B-14}$$

$p(x_0)$ is usually very small compare to $p(x_1)$ so $p(x_0)$ is usually neglected. Similar result is given by Wu and Katsube [21], except that they define $p(x)$ as $p(x_1) - p(x_0)$. $p(x)$ is also tabulated in Doyle [22]. The Exponential integral function can be expanded into an asymptotic series by integral by parts [23].

$$
\begin{aligned}
-Ei(-x) &= \int_x^{\infty} \frac{exp(-s)}{s} ds \\
&= \frac{exp(-x)}{x} - \int_x^{\infty} \frac{exp(-s)}{s^2} ds \\
&= \frac{exp(-x)}{x} - \frac{exp(-x)}{x^2} + 2\int_x^{\infty} \frac{exp(-s)}{s^3} ds \\
&= exp(-x)\left(\frac{1}{x} - \frac{1!}{x^2} + \frac{2!}{x^3} - \frac{3!}{x^4} \ldots + \frac{n!}{x^{n+1}}\right)
\end{aligned}
\tag{B-15}
$$

Then, $p(x)$ becomes

$$
\begin{aligned}
p(x) &= \frac{exp(-x)}{x} - \frac{exp(-x)}{x}\left(1 - \frac{1!}{x} + \frac{2!}{x^2} \ldots + \frac{n!}{x^n}\right) \\
&= \frac{exp(-x)}{x^2}\left(1! - \frac{2!}{x} \ldots + \frac{(n+1)!}{x^n}\right)
\end{aligned}
\tag{B-16}
$$

To quickly estimate the ending temperature T_1 (e.g. $C_1 = .05$), solve g by Eq. B-5 for a given n. Knowing the constant heating rate h, we can find x_1 by Eq. B-17, where $p(x)$ is approximated by the first term of Eq. B-16.

$$
g(x_1) = \frac{1}{h}\left(\frac{E_a}{R_g}\right)\left[\frac{exp(-x_1)}{x_1^2} - \frac{exp(-x_0)}{x_0^2}\right] \tag{B-17}
$$

Knowing x_1, we can calculate the ending temperature T_1 by $E_a/R_g/x_1$ (Eq. B-9), Another quick way to estimate the function g is two point (end point) approximation of the integral in Eq. B-8.

$$
g(T_1) = \frac{1}{2h}(T_1 - T_0)\left[exp(-\frac{E_a}{R_g T_1}) + exp(-\frac{E_a}{R_g T_0})\right] \tag{B-18}
$$

References

[1] Stokes, E.H., 1992, "Permeability of Carbonized Rayon Based Polymer Composites," AMD-Vol . 136, ASME, pp. 146-156.

[2] McManus, H. L. N., 1990, "High Temperature Thermo-Mechanical Behavior of Carbon-Phenolic and Carbon-Carbon Composites," Ph.D. Thesis, Stanford University, Stanford, CA.

[3] McManus, H. L. N., 1991, "Critical Factors in the Analysis of Decomposing Composites," AMD-Vol. 136, ASME, pp. 113-119.

[4] Keyhani, M. and Krishnan, V., 1992, "A One-Dimensional Model for the Thermal Response of a Decomposing Polymer," AMD-Vol . 136, ASME, pp. 81-90.

[5] Moyer, C.B., and Rindal, R., 1963, "An Analysis of the Coupled Chemically Reacting Boundary Layer and Charring Ablator," NASA contractor report NASA CR 1061.

[6] Henderson, J.B., Wiebelt, J.A., and Tant, M.R., 1985, "A Model for Thermal Response of a Polymer Composite Materials and Experimental Verification," *Journal of Composite Materials*, Vol 19, pp. 579-595.

[7] Henderson, J.B., and Wiecek, T.E., 1987, "A Mathematical Model to Predict the Thermal Response of Decomposing, Expanding Polymer Composites," *Journal of Composite Materials*, Vol 21, pp. 373-393.

[8] Florio, J., Henderson, J.B., and Miriyale, S.K., 1992, "Effect of Non-Thermal Equilibrium on the Thermally-Induced Response of Polymer Composites Exposed to High Heat Fluxes," AMD-Vol. 136, ASME, pp. 91-101.

[9] Kuhlmann, T.L., 1991, "Thermo-Chemical-Structural Analysis of Carbon-Phenolic Composites with Pore Pressure and Pyrolysis Effects," Ph.D. Thesis, University of California, Davis, CA.

[10] Sullivan, R. M., 1990, "A Finite Element Model for Thermo-Chemically Decomposing Polymers," Ph.D. Thesis, Pennsylvania State University, University Park, PA.

[11] Weiler, F. C., 1992, "Fully Coupled Thermo-Poro-Elasto Governing Equations," AMD-Vol . 136, ASME, pp. 1-28.

[12] Scheidegger, A. E., 1974, *The Physics of flow through porous media*, 3th edition, University of Toronto Press, Chapter 4.

[13] Sullivan, R. M., 1991, "A Coupled Solution Method for Predicting the Thermostructural Response of Decomposing, Expanding Polymeric Composites," AMD-Vol . 136, ASME, pp. 121-132.

[14] Biot, M.A., and Willis, D.G., 1957, "The Elastic Coefficients of the Theory of Consolidation," ASME J. of Applied Mechanics, Vol. 24, pp. 594-601.

[15] Tsai, S. W. and Hahn, T. H., 1980, *Introduction to Composite Materials*, Technomic Publishing Company, Chapter 8.

[16] Wylie, C. R. and Barret, L. C., 1982, *Advance Engineering Mathematics*, 5th edition, McGraw-Hill, Chapter 10.

[17] Sih, G. C., Michopoulos, J. G., and Chou, S. C., 1986, *Hygrothermoelasticity*, Martinus Nijhoff Publishers, Chapter 1.

[18] Reynolds, W. C., 1981, *Thermodynamic properties in SI*, Department of Mechanical Engineering, Stanford University.

[19] Beyer, W. H., 1985, *CRC Standard Mathematical Tables,* 27th Editions, CRC press.

[20] Stokes, E.H., 1987, "Moisture Diffusion in Carbon Phenolic Composites," JANNAF RNTS Meeting, MSFC, AL.

[21] Wu, Y. and Katsube, N., 1991, "Theoretical Predictions of FTE and RTG tests for Carbon-Phenolic Composites," AMD-Vol . 136, ASME, pp. 103-112.

[22] Doyle, C.D., 1961, "Kinetic Analysis of Thermogravimetric Data," *Journal of Applied Polymer Science*, Vol. 5, pp. 285-292.

[23] Lebedev, N. N., 1965, *Special Function and Their Applications*, Prentice-Hall, Section 3.2.